Interplay between electronic nematicity and elasticity in finite-size samples and surfaces

A THESIS
SUBMITTED TO THE FACULTY OF THE GRADUATE SCHOOL
OF THE UNIVERSITY OF MINNESOTA
BY

Aritra Lahiri

IN PARTIAL FULFILLMENT OF THE REQUIREMENTS
FOR THE DEGREE OF
MASTER OF SCIENCE

Prof. Rafael M. Fernandes

May, 2021

Acknowledgements

I would like to express my gratitude and deepest appreciation for my advisor, Prof. Rafael Fernandes, whose unwavering support has not only kept this work going, but also my prospective career alive. His way of advising is the right balance of carrots and sticks, with his constructive criticism playing a significant role in shaping my thoughts.

Additionally, I would like to thank Prof. Avraham Klein, whose insight and timely help have dramatically helped in formulating the problems and keeping me on the right track.

Abstract

In the phase diagram of iron-based superconductors, the proximity of superconductivity to electronic nematicity, the spontaneous breaking of the discrete rotational symmetry, has prompted numerous studies of a detailed understanding of nematicity and its interplay with superconductivity. Several studies have suggested the onset of nematic order above the bulk nematic critical temperature, along with indications of it being associated with the surface of the sample. In this work, motivated by the strong nemato-elastic interaction, we consider aspects of the interplay of elasticity and nematicity in realistic finite-size samples, considering both bulk and surface effects. First, we demonstrate non-trivial boundary effects in a finite-size sample, which significantly alter the order parameter profiles and the critical temperature. Elaborate finite-element simulations are carried out to solve the full nemato-elastic problem, demonstrating a strong inhomogeneity, dependent on the sample aspect ratio and geometric constraints. We find that the nematic critical temperature is bounded by the corresponding bulk value and, in fact, decreases rapidly with decreasing sample thickness, thereby necessitating the presence of other mechanisms to generate supercritical nematicity. We propose surface elastic disorder, such as domains of anisotropic defects, as possible avenues to realize supercritical nematicity. We show that these, in fact, lead to an incommensurate supercritical smectic state, localized at the sample surface, eventually transitioning into the standard uniform bulk nematic state. The smectic modulation wavevector is dependent only on the elastic parameters, and the coefficients entering the nematic free energy.

Contents

List of Figures

Chapter 1

Introduction

1.1 Motivation

One of the several enigmatic problems in physics is that of high-temperature superconductors (high-Tc SC), with the collective brilliance of the world yet to find a solution to the quest of achieving practical room temperature superconductivity. Currently, there are two main classes of high-Tc SCs, namely, copper-based (cuprates) and iron-based. In the iron-based superconductors (FeSC), superconductivity, and other associated electronic phenomena, take place in a quasi-two-dimensional layer consisting of Fe atoms bonded to phosphorus, arsenic, selenium or tellurium anions in a puckered chequerboard pattern as shown in Fig.1.1. FeSCs, like the cuprate superconductors, have a rich phase diagram with various competing as well as intertwined concomitant orders present alongside superconductivity [4, 5]. Particularly, superconductivity in FeSCs, in general, is found in proximity to an anti-ferromagnetically ordered ground state which, additionally, either coincides with or succeeds an electronic nematic state [6, 7, 8]. Such nematic signatures have also been observed in the intriguing pseudogap phase of the cuprates [9, 10, 11, 12, 13, 14, 15]. Nematicity, a term borrowed from liquid-crystal physics, is characterized by the spontaneous breaking of rotational symmetry of free space. Here, since the electrons reside on a square lattice, it involves the breaking of the discrete four-fold rotational symmetry, accompanied by a corresponding structural transition of the crystal lattice as illustrated in Fig.1.2, as well as an anisotropic electronic response. In the tetragonal crystal structure of the Fe-planes,

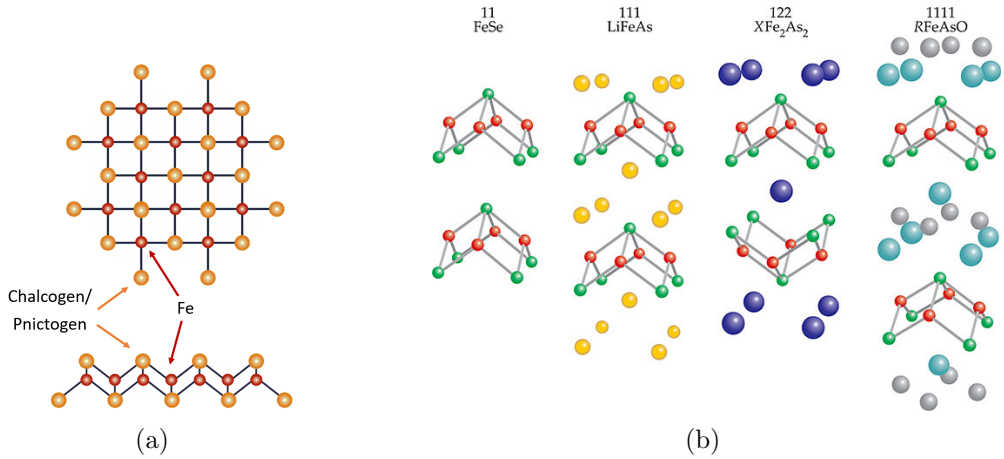

(a) (b)

Figure 1.1: (a) (Adapted from Ref. [1]) The two-dimensional tetragonal structure common to the crystal structure of all FeSCs in the high-temperature disordered phase, consisting of an Fe-layer with alternating chalcogen/pnictogen atoms lying above and below the Fe-plane. (b) (Adapted from Ref. [2]) The Fe-layers are either stacked by themselves in FeSe, or intercalated with spacer layers consisting of metallic complexes.

characterised by the D_{4h} point group, the nematic order belongs to either the B_{1g} or the B_{2g} irreducible representation, corresponding to an elongation along one of the in-plane principal ($x-, y-$axes), or diagonal axes, respectively. Experimental signatures of nematicity have been obtained using a variety of ways, such as neutron scattering [16, 17, 18, 19], transport measurements [20, 21], scanning tunnelling microscopy (STM) [6], and angle-resolved photoemission spectroscopy (ARPES) observations of broken orbital (d_{xz}/d_{yz}) degeneracy [22]. In the pursuit of the pairing glue for the unconventional superconductivity in FeSCs, the role of nematicity has been a prime topic of research due to its effect on superconductivity [23, 24, 25, 26, 27, 28, 29]. While nematicity has been shown to be originating from electronic degrees of freedom [8], there is nevertheless a significant symmetry-allowed coupling between the nematic order and lattice degrees of freedom [7, 30, 31, 32, 33, 34, 35, 36]. In general, bulk crystalline samples are twinned, with multiple nematic domains co-existing with each other. Experimental detection of nematicity, which is based on the anisotropy of observables, is thereby hindered due to the contributions from multiple domains canceling on average. Consequently, samples are typically de-twinned by applying uniaxial strain. However, this leads to a smooth growth of nematic order with decreasing temperature [20, 37], as it

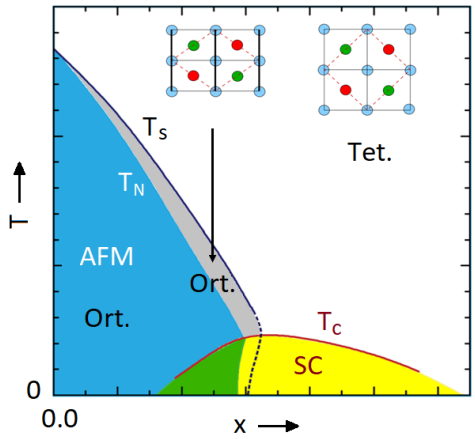

Figure 1.2: An illustration of the generic phase diagram in iron-based superconductors, as a function of temperature and another control parameters x, which could, for instance, be doping. The nematic phase (gray) precedes the (anti-ferro)magnetically ordered spin density wave (SDW) phase (blue). The nematic structural transition is marked and shown alongside, corresponding to B_{1g} nematicity. The light blue circles denote the Fe ions, while the green and red circles denote the As ions above and below the Fe plane, respectively.

constitutes an explicit breaking of in-plane discrete rotational symmetry. Interestingly, several experiments [38, 39, 40, 41, 42, 43, 44, 45, 46, 47, 48, 49, 50, 51, 52] conducted on un-strained samples have suggested the onset of nematicity $\approx 20 - 30K$ above the bulk nematic critical temperature, which we designate as supercritical nematic order. A critical feature with regard to these experiments is their differing sensitivity to surface and bulk physics. On the one hand, supercritical nematicity was suggested in ARPES [44, 45, 46], optical pump-probe spectroscopy [39, 43, 53] and STM [41] measurements, which are surface probes. On the other hand, no such evidence was found in specific heat measurements [54, 55], ruling out a bulk effect. In spite of significant evidence suggesting a surface phenomena, however, the situation is confounded by the indication of supercritical nematicity even in NMR [40] and torque magnetometry [38], which are bulk probes. Meanwhile, while theoretical studies on this aspect are lacking, Ref. [56] has investigated the possibility of supercritical surface nematicity due to the effect of inter-layer electronic tunneling in finite-size layered systems, in conjunction with the lattice degrees of freedom. In this study, motivated by these observations, as well as

the large nemato-elastic coupling, we perform a detailed investigation of the interplay between the elastic degrees of freedom and the electronic nematic order, focusing on both bulk and surface effects.

1.2 Interplay between nematicity and elasticity in finite-size samples

First, we study the coupled nemato-elastic problem in finite-size domains/samples using numerical finite element method (FEM) based simulations to solve the elastic problem. Our study is based on the Landau-Ginzburg paradigm, wherein distinct phases are characterised by their associated symmetries [57]. In this context, a phase transition involves a transition from an ordered to a disordered phase, with an order-parameter characterizing the reduction of symmetry. Subsequently, a coarse-grained effective action/free-energy is constructed using the order parameter, with the (non-zero) value of the order parameter uniquely identifying the broken symmetry phase. Specifically, for the nematic problem on a square lattice considered in this work, one obtains a field theory corresponding to a scalar nematic order parameter η which breaks a discrete $\mathbb{Z}_2$ symmetry,

$$F = \left(\frac{T - T_\eta^0}{2}\right)\eta^2 + \frac{b}{2}(\nabla\eta)^2 + \frac{u_\eta}{4}\eta^4, \tag{1.1}$$

where T_η^0 is the bare nematic critical temperature, b is the stiffness, and u_η is the quartic coupling. Now, the elastic degree of freedom is captured by the B_{1g} strain $\varepsilon = (\partial_x u_x - \partial_y u_y)/\sqrt{2}$ corresponding to the deformation field $\boldsymbol{u} = [u_x, u_y]$ and associated with the elastic constant $C = C_{11} - C_{12}$ (see Eq.(B.9) and Appendix B.6). In the presence of this B_{1g} strain, coupled to the nematic field via a bi-linear coupling g, one obtains,

$$F = \left(\frac{T - T_\eta^0}{2}\right)\eta^2 + \frac{b}{2}(\nabla\eta)^2 + \frac{u_\eta}{4}\eta^4 + \frac{C}{2}\varepsilon^2 - g\eta\varepsilon. \tag{1.2}$$

Typically, infinite systems with periodic boundary conditions are employed, which leads to uniform saddle-point solutions for the nematic and strain fields, with the bare nematic critical temperature renormalized/enhanced by an amount g^2/C. In our work, we consider a realistic finite-size sample, treating the elastic problem exactly using FEM simulations, and describe how boundary effects lead to non-trivial changes to the nematic field profile and the critical temperature. In general, the consideration of finite-size domains leads to boundary terms in the free energy which contribute to the boundary conditions for the nematic and strain fields. Additionally, the quartic term, in conjunction with the nematic stiffness, alter the nematic field profile and consequently the nematic critical temperature, when constrained by the boundary conditions. Taking note of these non-linear effects, an extensive numerical analysis is performed to study the coupled nemato-elastic problem in finite-size samples, and subsequently corroborated by analytical calculations, elucidating significant features due to non-linear effects arising from the boundary conditions and sample dimensions. Specifically, we demonstrate that in spite of the non-trivial finite-size effects, the enhancement of the nematic critical temperature is bounded by the corresponding enhancement in the thermodynamic limit, i.e., g^2/C. Additionally, in finite-size samples glued to a substrate, the nematic critical temperature decreases as the sample is made thinner. These results are intriguing in light of our initial goal of explaining the experimental observation of supercritical nematicity, which therefore entails an alternate mechanism.

1.3 Surface elastic step disorder induced smecticity

Finally, in order to explain the anomalous supercritical nematic signatures, we investigate the role of a specific class of lattice disorder, which exists primarily near the sample surface. Any such proposal must account for the significant variations across samples and experimental conditions, as the supercritical nematicity is not observed in all cases. In general, disorder is ubiquitous in most strongly correlated systems. Depending on the kind and strength of disorder as well as other dynamical factors, it may either smear out sharp transitions, completely destroy the phase transition and alter the ground state, induce slow glassy dynamics, or serve as a seed for certain ordered states. In particular, a number of studies have theoretically [58] and experimentally

[59, 41, 60, 61, 62] considered the impact of disorder on nematicity as well as superconductivity in FeSCs. Here, we propose a mechanism involving a specific kind of disorder, involving anisotropic surface defects such as domains of parallelly aligned steps, which are, for instance, created when crystals are cleaved. We show that such defects indeed lead to supercritical nematicity, which is in fact an incommensurate smectic state. This smectic state breaks translational symmetry in the direction perpendicular to the long axis of anisotropy of the defects, and decays exponentially into the bulk of the sample. The smectic modulation wavevector is determined by a combination of the elastic coefficients of the material and the coarse-grained Ginzburg-Landau parameters of the nematic free energy. Below the standard bulk nematic critical temperature, the bulk nematic state eventually dominates, washing away any signature of the supercritical smectic modulation. As such, this mechanisms leads to a unique situation where we witness a direct continuous transition from the isotropic to smectic phase.

Chapter 2

Coupled nematicity and elasticity in finite-size samples

2.1 Landau paradigm, boundary effects

The Landau paradigm has been a hallmark of modern condensed matter physics, wherein one describes phase transitions in terms of the associated symmetries, or lack thereof [57]. In this formulation, the short-distance microscopic degrees of freedom are traced out, leaving us with a coarse-grained action/free-energy, written as a functional of coarse-grained order parameters, representing collective degrees of freedom, and characterizing the reduction of symmetries on changing phases. The disordered high-temperature phase inherits the full symmetry group of the Hamiltonian, which is *spontaneously* broken to a sub-group in the low-temperature ordered phase. For instance, for a Heisenberg ferromagnet, the disordered phase is $O(3)-$symmetric corresponding to the full rotational symmetry of the spins, whereas the ferromagnetic phase has $O(2)$ symmetry. The order parameter, which gives the direction in which the magnetic axis is pointing, belongs to $O(3)/O(2) = S^2$. Similarly, the nematic phase transition, relevant to our study, involves the breaking of the four-fold discrete rotational symmetry C_4 in the square lattice to a two-fold C_2 symmetric state, with the order parameter belonging to the Ising class $C_4/C_2 = Z_2$. Subsequently, the optimal order parameter value, which being non-zero is representative of the broken symmetry phase, is obtained by the functional minimization of the free energy. For continuous phase transitions, one has the

free energy,

$$F = \int_M \left[\left(\frac{T - T_c}{2} \right) \eta^2 + \frac{b}{2} (\nabla \eta)^2 + \frac{u}{4} \eta^4] \right] \\ = \int_M \left[\left(\frac{T - T_c}{2} \right) \eta^2 - \frac{b}{2} \eta (\nabla^2 \eta) + \frac{u}{4} \eta^4 \right] + \int_{\partial M} \hat{n} \cdot \frac{b}{2} \eta (\nabla \eta), \tag{2.1}$$

where η is the order parameter, M denotes the spatial domain, ∂M denotes its boundary, and $\hat{n}$ is the oriented normal at the boundary. We restrict ourselves to continuous phase transitions, where there is no cubic term, and the quartic term is positive-definite. In homogeneous infinite space and/or domains with periodic boundary conditions, where the boundary contribution can be dropped, one obtains a spatially uniform solution on minimizing the free energy $\eta(T) = \sqrt{\frac{T_c - T}{u}} \Theta(T_c - T)$ with $\Theta(x)$ being the Heaviside-step function, thereby defining the critical temperature T_c below which $\eta \neq 0$. Now, in generic finite systems, the boundary terms generate boundary conditions on the order parameter profile. One may write $\eta = \eta_0 f(\boldsymbol{r})$, where $f(\boldsymbol{r})$ is a normalized ($\int_M f^2 = 1$) profile function satisfying the boundary conditions, characterizing the spatial dependence of η. This yields the bulk free energy,

$$F = F_{\text{bulk}} = \left[\left(\frac{T - T_c}{2} \right) - \frac{b}{2} \int_M f (\nabla^2 f) \right] \eta_0^2 + \frac{u}{4} \eta_0^4 \int_M f^4. \tag{2.2}$$

Clearly, the *saddle-point* critical temperature, T_c, at which the coefficient of the quadratic term vanishes, is now altered. If $\int_M f(\nabla^2 f) > 0$, which is the case when either the boundary conditions or some external potential or field enhance the field values (not explicitly specified here, but technically needs to be included), similar to a fluid preferably wetting the walls of its container, the critical temperature is raised. On the other hand, when $\int_M f(\nabla^2 f) < 0$, the situation is reversed and the critical temperature decreases. Note that, while the profile function f generally does depend on the non-linear quartic term, T_c is independent on it. This is because η increases continuously from zero at the critical temperature and hence, near T_c, the quartic term is negligibly small compared to the quadratic terms. As such, the profile function $f(\boldsymbol{r})$ must be ascribed an indirect temperature dependence, i.e., it must be specified as $f(\boldsymbol{r}, T)$. However, following the discussion above, we have that $f(\boldsymbol{r}, T_c)$ is independent of the quartic term. Hence, T_c is solely determined by the solution of the quadratic action. Similarly, in the case of

coupled order parameters, which is relevant to our study of coupled nematic and elastic fields, we have the action,

$$F = \int_M \left[\left(\frac{T - T_c}{2} \right) \eta^2 + \frac{b}{2} (\nabla \eta)^2 + \frac{u}{4} \eta^4 + \frac{C}{2} \varepsilon^2 - g \eta \varepsilon \right]. \tag{2.3}$$

Once again, using the normalized profile functions $\eta = \eta_0 f$ and $\varepsilon = \varepsilon_0 h$ satisfying the respective boundary conditions, we have,

$$F = \left[\left(\frac{T - T_c}{2} \right) - \frac{b}{2} \int_M f(\nabla^2 f) \right] \eta_0^2 + \frac{u}{4} \eta^4 \left(\int_M f^4 \right) + \frac{C}{2} \varepsilon_0^2 - g \eta_0 \varepsilon_0 \left(\int_M fh \right). \tag{2.4}$$

On minimising, we obtain $\varepsilon_0 = \left(\int_M fh \right) \frac{g}{C} \eta_0$. Thus,

$$F = \left[\frac{T - T_c}{2} - \frac{b}{2} \int_M f(\nabla^2 f) - \frac{g^2}{2C} \left(\int_M fh \right)^2 \right] \eta_0^2 + \frac{u}{4} \eta^4 \int_M f^4, \tag{2.5}$$

leading to a critical temperature renormalization equal to:

$$\Delta T_c = \frac{g^2}{C} \left(\int_M fh \right)^2 + b \int_M f(\nabla^2 f) = \frac{g^2}{C} \frac{\left(\int_M fh \right)^2}{(\int_M f^2)(\int_M h^2)} + b \int_M f(\nabla^2 f) \tag{2.6}$$

which differs from the expected value of $\frac{g^2}{C}$ in the absence of boundary effects. Even in the simplest case where the situation may permit one to neglect any significant variations (significant curvature with a large $\nabla^2 f$) in the nematic field profile f, we have by the Cauchy-Schwarz inequality, $\frac{\left(\int_M fh \right)^2}{(\int_M f^2)(\int_M h^2)} < 1$. As a result, the critical temperature enhancement is smaller than the corresponding value in the thermodynamic limit. Furthermore, the term $b \int_M f(\nabla^2 f)$ is in general negative and suppresses the critical temperature, unless there is some boundary phenomena leading to a preferential "wetting" behavior. As such, a proper study of realistic finite size samples entails a thorough investigation of sample geometry and boundary effects.

With this in mind, in this chapter we study the coupled nematic and elastic fields in a finite system, treating the elastic degrees of freedom exactly with a finite-element method-based solution for the strains. We begin by establishing the correct equations of motion and boundary conditions of the coupled system. Subsequently, we show that the nematic and strain field become inhomogeneous and more importantly, the nematic

critical temperature decreases as the sample is made thinner. These numerical results are supplemented by analytical approximations, revealing the scaling of the nematic critical temperature with the sample dimensions.

2.2 Action and Saddle-point equations

In this section, we introduce the electronic as well as geometric aspects of the problem, consisting of coupled nematic and strain fields, in a three-dimensional system with the bottom face glued to a substrate. There are two in-plane directions, x, y, and an out-of-plane direction z, normal to the sample surface at $z = 0$. The sample-substrate interface lies at $z = L_z$. The full three-dimensional action for the nematic field is taken as,

$$S = \int_M \left[\left(\frac{T - T_\eta^0}{2} \right) \eta^2 + \sum_{\mu=x,y,z} \frac{1}{2} b_\mu \left(\partial_\mu \eta \right)^2 + \frac{1}{4} u_\eta \eta^4 - g_{\text{el-nem}} \eta \varepsilon_{B_{1g}} + \frac{1}{2} C_{ijkl} \varepsilon_{ij} \varepsilon_{kl} \right] + \int_{\partial M} \left[\frac{1}{2} a^{s,\partial M} \eta^2 - g_{\text{el-nem}}^{s,\partial M} \eta \varepsilon_{B_{1g}} \right], \tag{2.7}$$

where M denotes the cuboid with dimensions $L_x \times L_y \times L_z$, T_η^0 is the bare nematic critical temperature, $b_{x,y,z}$ are the stiffness along the respective directions, u_η is the quartic energy coefficient, $g_{\text{el-nem}}$ is the nemato-elastic coupling, and C_{ijkl} are the elastic stiffness tensor elements/elastic constants. While this action introduces a generic setup, in our work we consider a tetragonal system with dimensions: $L_x = L_y = L_\parallel$ and $L_z = L$, as shown in Fig.2.1, and stiffness: $b_x = b_y = b_\parallel$ and $b_z = b$. In the following section, while deriving the equations of motion for the nematic field, we still formally distinguish the $x, y, z-$components for mathematical clarity, with the understanding that eventually the tetragonally symmetric choice is employed for all physical calculations. Finally, note that the nematic phase transition has been established to be of electronic origin [8] and hence, only the nematic mass $(T - T_\eta^0)$ has been ascribed an explicit temperature dependence, while the *bare* elastic constant and the nematic stiffness are temperature-independent constants. Lastly, we have also included surface contributions, namely, the surface nematic mass $a^{s,\partial M}$ and the surface nemato-elastic coupling $g_{\text{el-nem}}^{s,\partial M}$. Such surface terms arise from phenomena specific to the sample surface. They have to be explicitly included, separately from the bulk integral over the manifold M, as they are

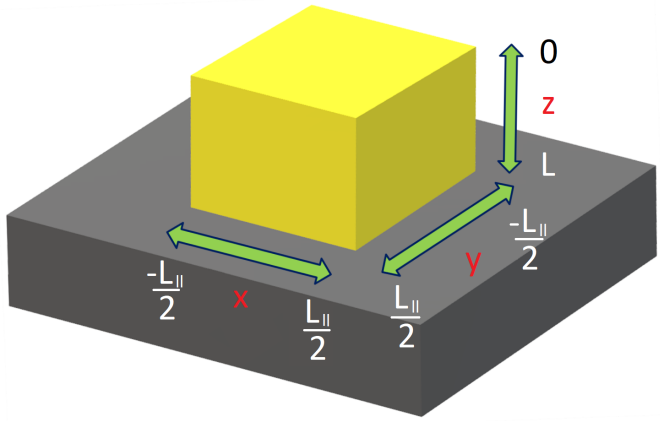

Figure 2.1: An illustration of the sample (yellow) of dimension $L_{\parallel} \times L_{\parallel} \times L$ glued to the substrate (dark gray). The coordinate axes and the locations are marked according to the convention employed in this work.

otherwise omitted from the continuum description in the variational procedure. This is because on moving from the discrete to the continuum formulation by constructing the Riemann integral, the surface contributions located on a thin layer at the surface form a measure zero set. Since the Riemann integral is "invisible" to functions with a measure zero support, the surface contribution escapes the action integral. Hence, if the contributions from the surface layers differ significantly, by which it is meant that it cannot be represented by the extrapolation of the function representing the bulk contribution, then they have to be explicitly added outside the integral. Such surface contributions have been investigated earlier in the context of magnetic and spin systems, for instance, see Refs. [63, 64, 65, 66, 67, 68]. However, we do not investigate the role of such surface contributions in this work and henceforth, we drop them.

2.2.1 Nematicity: Discrete formulation

First, the Euler-Lagrange/saddle-point equations for the nematic field are obtained using the discrete formulation of the variational principle in finite domains, as detailed in Appendix A.3. This approach has the advantage of being simple and lucid. The

discrete form of the action given by Eq. (2.7) is obtained as,

$$S = \sum_{j\in M}\prod_{\nu=1:3}\Delta_\nu\Bigg[\left(\frac{T-T_\eta^0}{2}\right)\eta_j^2 + \sum_{\mu=1}^{3}\frac{1}{2}b_\mu\left(\frac{\eta_j-\eta_{j+1_\mu}}{\Delta_\mu}\right)^2 + \frac{1}{4}u_\eta\eta_j^4 - g_{\text{el-nem}}\eta_j\varepsilon_{B_{1g},j}\Bigg] + \frac{1}{2}C_{ijkl}\varepsilon_{ij}\varepsilon_{kl}, \tag{2.8}$$

where, $M(\partial M)$ denotes the set of locations, indexed by $j \equiv [j_x, j_y, j_z]$, and lying in the bulk(on the surfaces). Furthermore, 1_μ denotes unit signed displacement by one lattice constant along the $\mu = x, y, z$ directions, for instance $1_x = [1, 0, 0]$, and $\Delta_\mu = |1_\mu|$ denotes the corresponding lattice constant. The last term involving the elastic energy is left untouched for now as we use the finite element method to tackle it. The saddle-point equations are readily obtained as follows:

• Bulk: For points lying in the bulk, every location, indexed by j, has two neighbors along each direction. Hence, two gradient terms, $\sum_{\mu=x,y,z}\left(\frac{\eta_j-\eta_{j-1_\mu}}{\Delta_\mu}\right)^2 + \left(\frac{\eta_j-\eta_{j+1_\mu}}{\Delta_\mu}\right)^2$, contribute to the functional derivative with respect to η_j. Therefore, we obtain,

$$\sum_{\mu=x,y,z} -b_\mu\frac{\eta_{j+1_\mu}+\eta_{j-1_\mu}-2\eta_j}{\Delta_\mu^2} + (T-T_C^\eta)\eta_j + u_\eta\eta_j^3 - g_{\text{el-nem}}\varepsilon_{B_{1g},j} = 0. \tag{2.9}$$

• Boundaries: We show the equations explicitly only for one boundary element, while the corresponding equations for the remaining elements are obtained by replacing the coordinate dependent quantities with their corresponding counterparts.

– Surface: For points lying on the surface at $x = L_\parallel/2$, without loss of generality, every location j has two neighbors along $y-, z-$directions but only one neighbor along the $x-$direction. Hence, the terms with a non-zero contribution to the functional derivative with respect to η_j are,

$$S_j = \Delta_x\Delta_y\Delta_z\Bigg[\frac{1}{2}b_x\left(\frac{\eta_{[N,j_y,j_z]}-\eta_{[N-1,j_y,j_z]}}{\Delta_x}\right)^2 + \sum_{\substack{\mu=y,z\\ \sigma=\pm1}}\frac{1}{2}b_\mu\left(\frac{\eta_{[N,j_y,j_z]}-\eta_{[N,j_y,j_z]-\sigma1_\mu}}{\Delta_\mu}\right)^2 - g_{\text{el-nem}}\varepsilon_{B_{1g},j_x=N}\Bigg]. \tag{2.10}$$

On setting the function derivative $\frac{\partial S}{\partial \eta_{[N,j_y,j_z]}}$ to zero, and multiplying throughout by Δ_x, we obtain,

$$\left[b_x \frac{\eta_{[N,j_y,j_z]} - \eta_{[N-1,j_y,j_z]}}{\Delta_x}\right] + \Delta_x \sum_{\mu=y,z} b_\mu \left\{ \frac{2\eta_{[N,j_y,j_z]} - \eta_{[N,j_y,j_z]-1_\mu} - \eta_{[N,j_y,j_z]+1_\mu}}{\Delta_\mu^2} \right\}$$
$$- \Delta_x g_{\text{el-nem}} \varepsilon_{B_{1g},[N,j_y,j_z]} = 0. \tag{2.11}$$

In the continuum limit, setting $\Delta_\mu \to 0$, we simply obtain the Neumann condition $b_x \frac{\partial \eta}{\partial x} = 0$. This is exactly the boundary derivative generated from integrating by parts (to be shown in the next sub-section), as obtained when performing the variational procedure in the continuum description from the beginning. In the discrete formulation given by Eq.(2.11), it is seen that the contributions of the second derivative along the directions lying on the surface, as well as the strain, are suppressed by an additional factor of Δ_x. As such, they vanish in the continuum limit. Nevertheless, we do retain these suppressed contributions in our numerical calculations, which allows for the correct scaling with increasing lattice resolution. Additionally, the contribution of the quartic term also vanishes due to the same reason. We do not, however, retain that, as it would complicate the calculation of the boundary values. In any case, near the critical temperature, its contribution is expected to be negligible. Finally, we have,

$$\eta_{[N,j_y,j_z]} = \frac{\frac{b_x}{\Delta_x^2}\eta_{[N-1,j_y,j_z]} + \frac{b_y}{\Delta_y^2}\left(\eta_{[N,j_y-1,j_z]} + \eta_{[N,j_y+1,j_z]}\right) + \frac{b_z}{\Delta_z^2}\left(\eta_{[N,j_y,j_z-1]} + \eta_{[N,j_y,j_z+1]}\right)}{\frac{b_x}{\Delta_x^2} + 2\frac{b_y}{\Delta_y^2} + 2\frac{b_z}{\Delta_z^2}}. \tag{2.12a}$$

– Edge:

$$\eta_{[N,N,j_z]} = \frac{\frac{b_x}{\Delta_x^2}\eta_{[N-1,N,j_z]} + \frac{b_y}{\Delta_y^2}\eta_{[N,N-1,j_z]} + \frac{b_z}{\Delta_z^2}\left(\eta_{[N,N,j_z-1]} + \eta_{[N,N,j_z+1]}\right)}{\frac{b_x}{\Delta_x^2} + \frac{b_y}{\Delta_y^2} + 2\frac{b_z}{\Delta_z^2}}. \tag{2.13}$$

– Vertex:

$$\eta_{[N,N,N]} = \frac{\frac{b_x}{\Delta_x^2}\eta_{[N-1,N,N]} + \frac{b_y}{\Delta_y^2}\eta_{[N,N-1,N]} + \frac{b_z}{\Delta_z^2}\eta_{[N,N,N-1]}}{\frac{b_x}{\Delta_x^2} + \frac{b_y}{\Delta_y^2} + \frac{b_z}{\Delta_z^2}}. \tag{2.14}$$

2.2.2 Nematicity: Continuum formulation

Now, we complement the previously adopted discrete approach with the more common approach of adopting the continuum formulation from the outset. The fundamental principle is described in Appendix A.1, which we do not repeat here. Beginning with Eq. (2.7), and ignoring the free elastic energy, the nematic action is given by,

$$S = \int_M \left[\frac{T - T_\eta^0}{2}\eta^2 + \sum_{\mu=x,y,z} \frac{1}{2} b_\mu \big(\partial_\mu \eta\big)^2 + \frac{1}{4} u_\eta \eta^4 - g_{\text{el-nem}} \eta \varepsilon_{B_{1g}} \right]. \tag{2.15}$$

Now, following Appendix A.1, on setting the functional variation of the action with respect to η, $\delta S = \int_M d^3\boldsymbol{r} \big[\frac{\delta \mathcal{L}}{\delta \eta}\delta\eta + \frac{\delta \mathcal{L}}{\delta \partial_\mu \eta}\delta\partial_\mu\eta \big]$, to zero, we obtain,

$$\int_M \Big[(T - T_\eta^0)\eta + u_\eta \eta^3 - \sum_{\mu=x,y,z} b_\mu \big(\partial_\mu^2 \eta\big) - g_{\text{el-nem}} \varepsilon_{B_{1g}} \Big] \delta\eta + \sum_{\mu=x,y,z} \int_{\partial M} b_\mu (\partial_\mu \eta) \delta\eta \big|_{\min \boldsymbol{r}_\mu}^{\max \boldsymbol{r}_\mu} = 0, \tag{2.16}$$

where we have integrated by parts to separate the expression into a bulk integral and boundary terms. Also, $\hat{n}^\mu$ is the μ^{th} component of the outward oriented normal $\hat{n}$ of the sample surface, and min/max $\boldsymbol{r}_\mu$ denotes the lower and upper limit of the $\mu^{\text{th}}-$coordinate. Note that both the bulk and the boundary contributions must vanish, independently. Thus, we obtain Neumann boundary condition at all faces, where the nematic field gradient normal to the surface vanishes. The equations are explicitly shown in Fig.2.2 at their corresponding location of applicability.

2.2.3 Elasticity: Continuum formulation

Before obtaining the equations of motion for the elastic degrees of freedom, we take a moment to introduce the elastic constants, as well as alternate ways of specifying them,

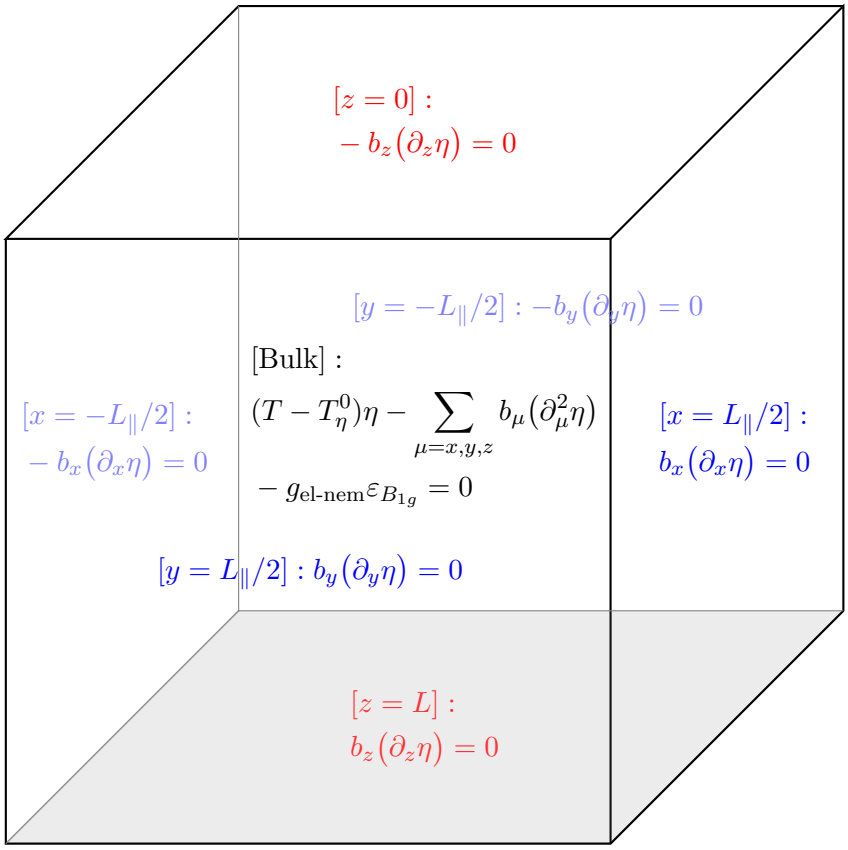

Figure 2.2: The bulk equation of motion and the surface boundary condition for the nematic field in a cuboidal sample, at their respective regions of applicability. The shaded bottom face represents the sample-substrate interface. All the faces have Neumann conditions. Note that, in this work we use $b_x = b_y = b_\parallel$, and $b_z = b$.

as used in this work. While this is discussed in detail in Appendix B.3, we nevertheless state it here for convenience. For an isotropic material, in the Voigt notation (described in Appendix B.3), we have,

$$C_{11} = C_{22} = C_{33} = \lambda + 2\nu = \frac{E(1-\nu)}{(1+\nu)(1-2\nu)}, \tag{2.17a}$$

$$C_{12} = C_{13} = \lambda = \frac{E(\nu)}{(1+\nu)(1-2\nu)}, \tag{2.17b}$$

$$C_{44} = C_{55} = C_{66} = \frac{C_{11} - C_{12}}{2} = \mu = \frac{E}{2(1+\nu)}, \tag{2.17c}$$

where λ and μ are the Lamé parameters, while E and ν denote the Young′s modulus and the Poisson′s ratio, respectively. We primarily use the description in terms of the elastic constants in our work. However, the numerical solution, as described later in this chapter, relies on the alternate description in terms of the Young′s modulus and Poisson′s ratio. Additionally, we consider an isotropic material (described in Appendix B.3) in this work for simplicity, which does not affect the results qualitatively. While the elastic constants C_{11}, C_{12}, C_{44}, and C_{55} are not independent of each other due to the relation $C_{44} = C_{55} = C_{66} = (C_{11} - C_{12})/2$ in isotropic materials, we do refer to it as C_{44} in later stages of this work, for clarity.

Now, for the elasticity problem, we straightaway begin with the continuum formulation for brevity. The equivalence of the discrete and continuum approaches was already shown previously for the nematic fields, which holds in this case too. We consider an isotropic material, as introduced in Appendix B.3, with the action,

$$S = \int d^3\boldsymbol{r} \frac{1}{2} C_{ijkl}\varepsilon_{ij}\varepsilon_{kl} - g_{\text{el-nem}}\eta \frac{1}{\sqrt{2}}(\partial_x u_x - \partial_y u_y), \tag{2.18}$$

where u_i is the i^{th} component of the deformation field $\boldsymbol{u}$, and $\varepsilon_{ij} = \frac{1}{2}(\partial_i u_j + \partial_j u_i)$ is the strain field. The nematic field η couples to the B_{1g} deformation $\frac{1}{\sqrt{2}}(\partial_x u_x - \partial_y u_y)$. We have chosen the normalization factor of $1/\sqrt{2}$ as it yields the normalized B_{1g} strain eigenvector with the eigenvalue $C = C_{11} - C_{12}$, as described in Appendix B.6. An important remark must be made regarding the choice of field variables. Typically, the action is written in terms of the strain fields (see, for instance, Refs. [69, 5, 70]),

$$S = \frac{1}{2} C\varepsilon_{B_{1g}}^2 - g_{\text{el-nem}}\eta\varepsilon_{B_{1g}} \xrightarrow{\text{saddle-point}} C\varepsilon_{B_{1g}} = g_{\text{el-nem}}\eta. \tag{2.19}$$

However, at a more fundamental level, one must use a displacement formulation where the action is written in terms of the deformation fields $\boldsymbol{u}$, as it ensures strain compatibility, and the numerical FEM solutions work using the deformation fields. We show the equivalence between these two approaches in the next section. Now, the saddle-point equations of motion (EOM) in the displacement formulation are obtained be setting the

functional variation in the action $\delta S = \int_M d^3\boldsymbol{r}\big[\frac{\delta\mathcal{L}}{\delta u_i}\delta u_i + \frac{\delta\mathcal{L}}{\delta\partial_j u_i}\delta\partial_j u_i\big]$ to zero. This yields,

$$\delta S = \int_M d^3\boldsymbol{r}\big[-\partial_j C_{ijkl}\partial_l u_k\big]\delta u_i + \int_M d^3\boldsymbol{r}\frac{g_{\text{el-nem}}}{\sqrt{2}}\big[(\partial_x\eta)\delta u_x - (\partial_y\eta)\delta u_y\big] \\ - \int dydz\frac{g_{\text{el-nem}}\eta}{\sqrt{2}}\delta u_x\big|_{-L_\parallel/2}^{L_\parallel/2} + \int dxdz\frac{g_{\text{el-nem}}\eta}{\sqrt{2}}\delta u_y\big|_{-L_\parallel/2}^{L_\parallel/2} + \int_{\partial M} d^2\boldsymbol{r}\hat{n}_j\big[C_{ijkl}\partial_l u_k\big]\delta u_i = 0, \tag{2.20}$$

where, similar to the previously studied case of the nematic action, we have integrated by parts to separate the expression into bulk integrals (first line), which form the equations of motion, and boundary terms (second line) which constitute the set of boundary conditions. In the last term, we have $\hat{n}_x(-L_\parallel/2) = -\hat{x}$, $\hat{n}_x(L_\parallel/2) = \hat{x}$, $\hat{n}_y(-L_\parallel/2) = -\hat{y}$, and $\hat{n}_y(L_\parallel/2) = \hat{y}$. Note that the effect of uniform bulk nematicity shows up only through the boundary conditions at the $x = \pm L_\parallel/2$ and $y = \pm L_\parallel/2$ planes (shown in blue) acting like externally applied stresses. However, in general, inhomogeneous nematicity also couples to the bulk deformations. Consequently, the top face of the sample has zero-stress boundary condition, while the vertical faces have an effective applied stress specified by the nematic field. At the sample-substrate interface at $z = L$, where the sample is fixed to the substrate, we have the Dirichlet condition, where the deformations vanish. One should ideally include an extra constraint/term which forces the deformation to vanish. We do not explicitly show that in the action and instead, directly apply the boundary condition $\boldsymbol{u}(L) = 0$. In essence, this amounts to assuming a very stiff and large substrate, which exerts a much stronger effect than the Neumann boundary conditions derived above. Additionally, this Dirichlet condition at the sample-substrate interface stabilizes the action against arbitrary constant shifts, which is otherwise dependent only on the derivatives of $\boldsymbol{u}$. The final set of equations and boundary conditions, at their respective locations of applicability, are shown in Fig.2.3.

Uniform nematicity: Equivalence of displacement and strain approaches

Here, we show the equivalence of the results obtained using the displacement formulation, and the commonly employed strain formulation mentioned earlier in Eq.(2.19), for the simple case of uniform nematicity. We consider an infinitely long sample with

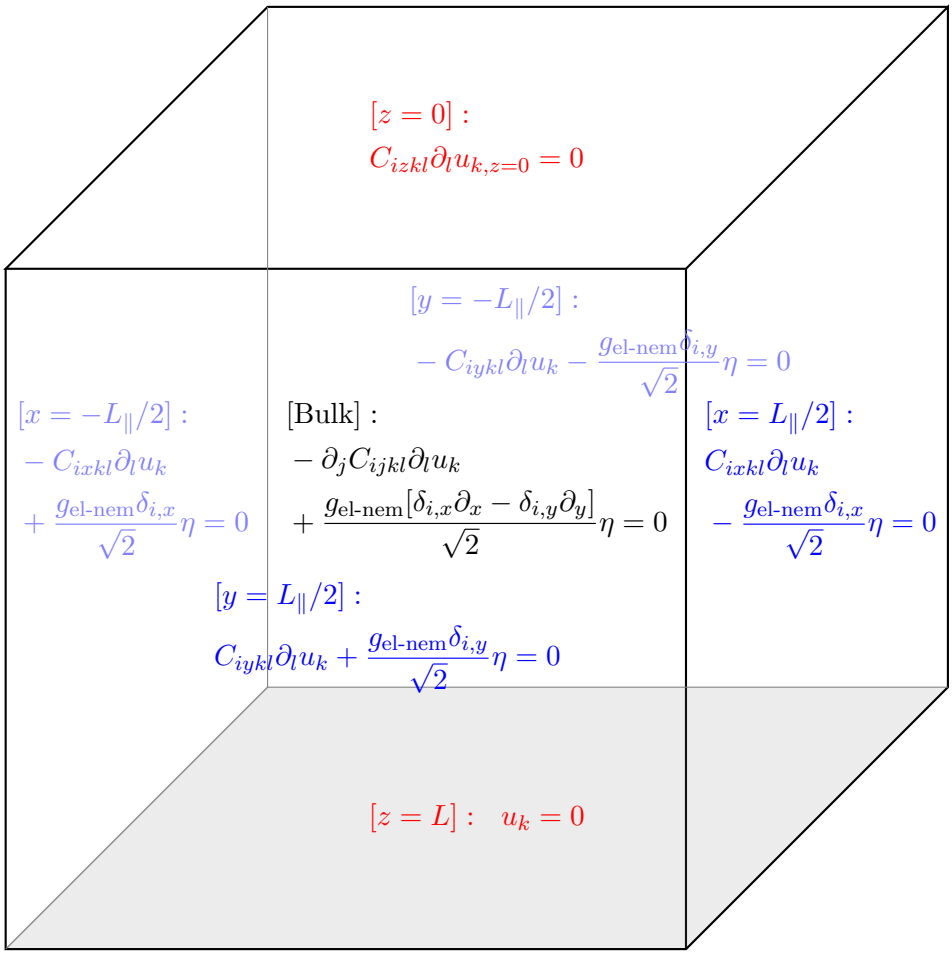

Figure 2.3: The bulk equation of motion and the surface boundary condition for the deformation fields in a cuboidal sample, at their respective regions of applicability. The shaded bottom face represents the sample-substrate interface with the Dirichlet condition. The top face has zero-stress condition, while the stress at the vertical faces is specified by the corresponding nematic field value.

$L \to \infty$ which, in conjunction with the lack of any sources conjugate to u_z and derivatives of u_z, results in $u_z = 0$ and the remaining deformations being uniform along the $z-$direction. In this case, with uniform nematicity, the bulk equations in a tetragonal system (see Appendix B.3) simply become,

$$C_{11}\partial_x^2 u_x + C_{12}\partial_x\partial_y u_y + C_{13}\partial_x\partial_z u_z + C_{66}\partial_y^2 u_x = 0, \tag{2.21a}$$

$$C_{11}\partial_y^2 u_y + C_{12}\partial_x\partial_y u_x + C_{13}\partial_y\partial_z u_z + C_{66}\partial_x^2 u_y = 0, \tag{2.21b}$$

$$C_{33}\partial_z^2 u_z + C_{13}\partial_z\partial_x u_x + C_{13}\partial_z\partial_y u_y + C_{44}[\partial_z u_x + \partial_x u_z] + C_{44}[\partial_z u_y + \partial_y u_z] = 0. \tag{2.21c}$$

The boundary conditions are,

$[x = \pm L_\parallel/2]$:

$$C_{11}\partial_x u_x + C_{12}\partial_y u_y + C_{66}(\partial_x u_y + \partial_y u_x) + C_{44}(\partial_x u_z + \partial_z u_x) = \frac{g_{\text{el-nem}}\eta}{\sqrt{2}}, \tag{2.22a}$$

$$C_{66}(\partial_x u_y + \partial_y u_x) = 0, \tag{2.22b}$$

$$C_{44}(\partial_x u_z + \partial_z u_x) = 0, \tag{2.22c}$$

$[y = \pm L_\parallel/2]$:

$$C_{11}\partial_y u_y + C_{12}\partial_x u_x + C_{66}(\partial_x u_y + \partial_y u_x) + C_{44}(\partial_y u_z + \partial_z u_y) = \frac{-g_{\text{el-nem}}\eta}{\sqrt{2}}, \tag{2.22d}$$

$$C_{66}(\partial_x u_y + \partial_y u_x) = 0, \tag{2.22e}$$

$$C_{44}(\partial_y u_z + \partial_z u_y) = 0. \tag{2.22f}$$

Motivated by the intuitively expected solution, the solution is checked to be given by,

$$u_x = \frac{g_{\text{el-nem}}\eta}{\sqrt{2}(C_{11} - C_{12})}x, \quad u_y = -\frac{g_{\text{el-nem}}\eta}{\sqrt{2}(C_{11} - C_{12})}y. \tag{2.23a}$$

$$\implies \varepsilon_{B_{1g}} = \frac{\partial_x u_x - \partial_y u_y}{\sqrt{2}} = \frac{g_{\text{el-nem}}\eta}{(C_{11} - C_{12})}, \tag{2.23b}$$

as expected from Eq.(2.19). The uniqueness of boundary value problems guarantees this to be the unique solution.

2.3 Numerical solution

Here, we numerically solve the full three-dimensional elasto-nematic problem. The procedure is schematically depicted in Fig.2.4. The solution begins with the construction of an initial guess for the nematic and strain fields using analytical plate-theoretic ansatz, with a linearly varying strain profile across the sample thickness. The subsequent calculation is performed on MATLAB®, utilizing its finite-element method (FEM) package in its partial differential equation toolbox. In the following sub-sections, we describe the solution to the elastic and nematic problems, separately.

2.3.1 Strain

FEM

First, for the FEM solution of the strain field, we cast our expressions in the form $m\frac{\partial^2 u}{\partial t^2} + d\frac{\partial u}{\partial t} - \nabla\cdot(C\nabla u) + au = f$. The bulk equation of motion for the strain field Eq. (2.20) is cast in this form with $m = d = a = 0$, with C being the elastic stiffness tensor. Now, $f = \frac{g_{\text{el-nem}}[\delta_{i,x}\partial_x - \delta_{i,y}\partial_y]}{\sqrt{2}}\eta$ is derived from the nematic field, as detailed in Fig.2.3. Finally, the boundary conditions are required in the form $\vec{n}\cdot(C\nabla u) + qu = g$. Using Eq. (2.20), we obtain,

$$\boldsymbol{g} = \left[\frac{g_{\text{el-nem}}\eta}{\sqrt{2}}\big(\delta_{x,L_x} - \delta_{x,0}\big), -\frac{g_{\text{el-nem}}\eta}{\sqrt{2}}\big(\delta_{y,L_y} - \delta_{y,0}\big), 0\right]; \quad (z \neq L) \tag{2.24a}$$

along with $q = 1$ only at $z = L_z$, where $\boldsymbol{g} = 0$, to enforce the Dirichlet condition at the sample-substrate interface.

Lastly, a quick note is made regarding the actual elastic stiffness tensor. We consider an isotropic material in this work without loss of generality, with the Lamé parameters λ, μ defined in terms of the Young's modulus E and Poisson's ratio ν: $\lambda = E\nu/((1+\nu)(1-2\nu))$ and $\mu = E/(2(1+\nu))$. Hence, the B_{1g} elastic constant is $C = C_{11} - C_{12} = (\lambda + 2\mu) - \lambda = 2\mu = E/(1+\nu)$. In this work, we have arbitrarily chosen $E = 5C/4$ and $\nu = 1/4$. Henceforth, we interchangeably describe the elastic properties in terms of the elastic constants, as well as the Young's modulus and Poisson's ratio, as the numerical FEM solution in MATLAB® requires the latter as its input. Our analytical results, however, are primarily stated in terms of the former.

2.3.2 Nematicity

For the nematic field, we use a relaxation based iterative method to solve the non-linear system Eqs. (2.9),(2.12), (2.13), (2.14). The new bulk field values in the $(j+1)^{\text{th}}$ iteration (LHS) are found from the old field values in the j^{th} iteration (RHS) by the backward Euler method. The boundary conditions are imposed by setting the boundary values of the nematic field after every iteration, based on Eqs. (2.12), (2.13) and (2.14).

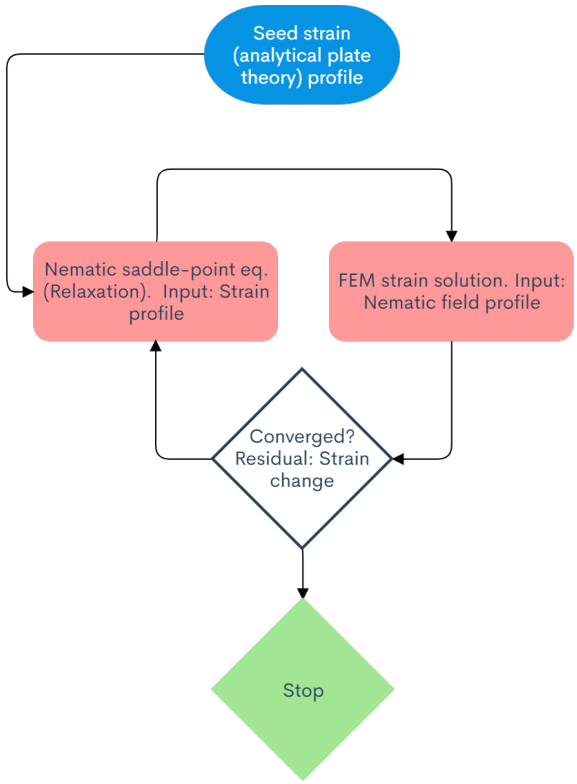

Figure 2.4: A flowchart depicting the self-consistent numerical solution to the nematic Ginzburg-Landau and strain FEM equations. The seed is obtained using analytical plate theory, as detailed in Appendix B.7, where a strain profile varying linearly across the sample thickness is used.

2.3.3 Results

Here we describe the observations of our numerical calculations. To set the system dimensions, we refer to the experimental setups where the typical sample dimensions are approximately $L_x \approx L_y = L_\parallel = \alpha L$, with $2 \lessapprox \alpha \lessapprox 30$. Specifically, in Ref. [54]: $130\mu m$, $180\mu m$, $13\mu m$, and $120\mu m$, $110\mu m$, $20\mu m$; in Ref. [38]: $70\mu m$, $70\mu m$, $30\mu m$, and in Ref.[71]: $3000\mu m$, $3000\mu m$, $100\mu m$. In the following sections, we consider three cases:

- An effective one-dimensional set-up with in-plane uniform nematicity and strain.
- A quasi one-dimensional set-up with in-plane uniform nematicity, but the full three-dimensional FEM-based strain.
- The full three-dimensional nematicity and FEM-based strain. Note that, in the limit of infinite nematic stiffness, this reduces to the previous case.

Before we describe the three cases in detail, we present in Fig.2.5 the variation of the critical temperature for the first and the third cases considered above, corresponding to the green, and blue curves, respectively. We also show the strain and nematic field profiles, highlighting the inhomogeneities. To obtain the numerical values for the critical temperature shown in Fig.2.5, we extrapolate the corresponding values obtained on a series of systems with increasing lattice discretization, as described in Appendix C.

One-dimensional in-plane uniform nematicity and strain

Here we begin with the simplest case, where we consider in-plane uniform nematic and strain fields, which precludes any boundary effects from the vertical faces of the sample. Such in plane uniformity of the nematic field is naturally realized in the $b_{x,y} \to \infty$ limit. However, as it shall be clear from the subsequent sections, the in-plane uniformity for the strain field is, strictly speaking, artificial. It constitutes a good approximation only for sufficiently thick samples with $L_z \gtrapprox L_\parallel$, where the elastic boundary effects from the vertical faces of the sample are minimal.

A detailed description of the form of the strain field and the nematic critical temperature T_η, is presented later in Eqs. (2.34), (2.35), and the associated text. Importantly, we obtain an effectively enlarged B_{1g} elastic constant $C + C_{44}\frac{L_\parallel^2}{L^2}\frac{\pi^2}{48}$, thereby causing

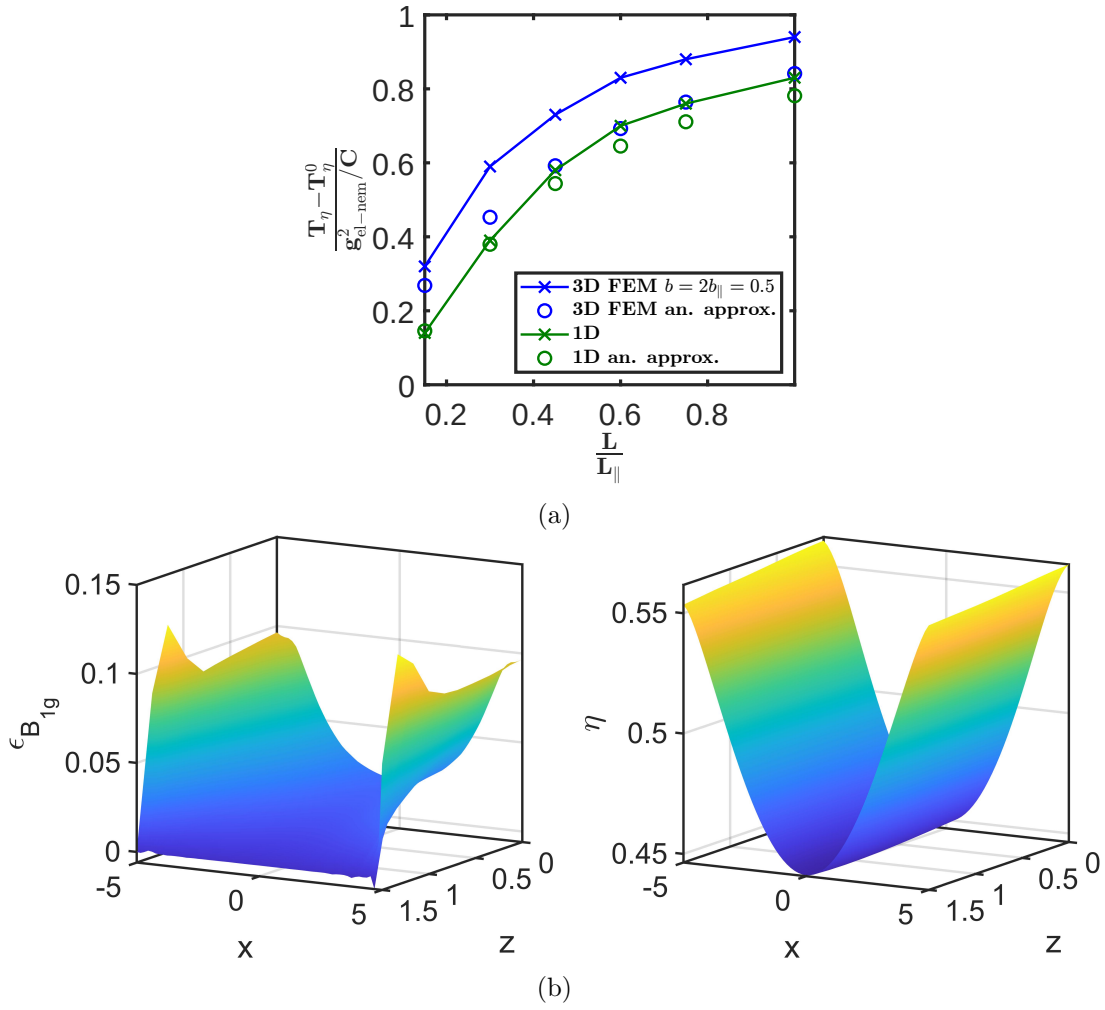

Figure 2.5: (a) Variation of the nematic critical temperature T_η with the thickness of the sample L, where $b = 0.5$, $b_x = b_y = 0.25$, $N_z = 10$, $N_x = N_y = 65$, $C = 0.5$, $g_{\text{el-nem}} = \sqrt{0.1C}$, and $u_\eta = 0.1$. The blue circles represent the analytical approximation obtained in Eq.(2.46) and Fig.2.7. Finally, the green curve corresponds to the purely one-dimensional case where both the nematic and strain fields are in-plane constant, and the green circles represent Eq. (2.34), which is an analytical approximation corresponding to this case. (b) The profiles of the strain (left) and the nematic (right) fields, with $L_\parallel = 10$, $L = 1.5$ and $T = 0.05$, highlighting the significant inhomogeneities. In particular, the strain vanishes at the sample-substrate interface at $z = L = 1.5$, and grows sharply near the vertical faces located at $x = \pm L_\parallel/2 = \pm 5$.

the critical temperature to decrease as the sample is made thinner. Additionally, the critical temperature also decreases on increasing the nematic stiffness b, although the variation is limited to $\approx 20\%$ of the $b = 0$ value as b spans $[0, \infty)$.

One-dimensional in-plane uniform nematicity, exact three-dimensional strain

Now, we again consider in-plane constant nematic field while obtaining the full three-dimensional strain field using FEM. As we shall describe in the subsequent sections, the strain experiences boundary enhancements at the vertical faces of the sample, which is partially incorporated in the current formulation without the feedback from the nematic field. The action is given by,

$$S = L_{\parallel}^2 \int_z \left[\left(\frac{T - T_\eta^0}{2} \right) \eta^2 + \frac{b}{2} (\partial_z \eta)^2 + \frac{u_\eta}{4} \eta^4 - g_{\text{el-nem}} \eta \frac{\iint_{x,y} \varepsilon_{B_{1g}}}{L_{\parallel}^2} \right] + S_\varepsilon, \tag{2.25}$$

where, S_ε is the action of the free strain fields, and we have used the assumption that the nematic field is in-plane uniform. We have not stated the form of the elastic action S_ε as the strain fields are obtained from a numerical FEM solution, which directly enters the saddle-point equation for the nematic field as shown below,

$$\begin{aligned} &- b \frac{\eta_{[j_x, j_y, j_z+1]} + \eta_{[j_x, j_y, j_z-1]} - 2\eta_{[j_x, j_y, j_z]}}{\Delta_z^2} + (T - T_C^\eta) \eta_{[j_x, j_y, j_z]} + u_\eta \eta_{[j_x, j_y, j_z]}^3 \\ &- g_{\text{el-nem}} \frac{\sum_{j_x . j_y} \varepsilon_{B_{1g}, [j_x, j_y, j_z]}}{N_{\parallel}^2} = 0. \end{aligned} \tag{2.26}$$

Here $N_\parallel$ is the number of lattice sites along the $x-$ and $y-$ directions. This equation is solved self-consistently with the FEM equations, with the necessary steps involving the FEM solution described in Sec.2.3.

In contrast to the previously performed purely one-dimensional solution assuming in-plane uniformity for both the nematic and strain fields, remarkably the strains are enhanced at the vertical boundary faces of the sample. This is explicitly seen in the cross-sectional profile of the strain field in Fig.2.6, where we have used an illustrative nematic field $\eta(x, y, z) = 0.3\big[\cos(\pi z/L) + 1\big]$, which satisfies the required boundary conditions described in Fig.2.2. It is uniform in the plane, and it is the first/simplest harmonic along the $z-$direction satisfying the Neumann conditions at $z = 0$ and $z =$

L. Lastly, the magnitude of the constant term is arbitrarily chosen, as it does not qualitatively impact the variation of the strain field in the $x, y-$directions. Now, as a result of the boundary enhancement of the strain fields, the critical temperature is higher than the value obtained from a purely one-dimensional solution. Since the nematic field is constant in the plane, at each z, it is subjected to the mean in-plane strain at that value of z. Beginning with the action given by Eq.(2.25), we formally specify the solution for the strain field as $\langle \varepsilon_{B_{1g},\mathrm{3D}} \rangle = f_{\mathrm{3D}}(\boldsymbol{r}, \eta, C)$ and $\langle \varepsilon_{B_{1g},\mathrm{1D}} \rangle = f_{\mathrm{1D}}(z, \eta, C)$, where the subscripts 3D and 1D denote the full-three dimensional FEM-based strain incorporating the boundary conditions exactly, and the effectively one-dimensional in-plane constant strain mentioned in the previous section, respectively. As described in Fig.2.6 and the associated text, $\frac{1}{L_\parallel^2}\int_{x,y} f_{\mathrm{3D}}(\boldsymbol{r}, \eta, C) > \frac{1}{L_\parallel^2}\int_{x,y} f_{\mathrm{1D}}(z, \eta, C) = f_{\mathrm{1D}}(z, \eta, C)$, for the same η and z. Furthermore, using the facts that the strain must vanish when $\eta = 0$, and $\eta \to -\eta$ implies $\varepsilon \to -\varepsilon$, the functions f_{1D} and f_{3D} are expanded as follows,

$$f_{\mathrm{1D}}(z, \eta, C) = f_{\mathrm{1D}}^{(1)}(z, C)\eta_z + f_{\mathrm{1D}}^{(3)}(z, C)\eta_z^3 + \ldots, \tag{2.27a}$$

$$f_{\mathrm{3D}}(\boldsymbol{r}, \eta, C) = f_{\mathrm{3D}}^{(1)}(\boldsymbol{r}, C)\eta_z + f_{\mathrm{3D}}^{(3)}(\boldsymbol{r}, C)\eta_z^3 + \ldots. \tag{2.27b}$$

Note that, as described in Fig.2.6, $\frac{1}{L_\parallel^2}\int_{x,y} f_{\mathrm{3D}}(\boldsymbol{r}, \eta, C) > f_{\mathrm{1D}}(z, \eta, C)$ for arbitrarily small values of η_z and thus, $\frac{1}{L_\parallel^2}\int_{x,y} f_{\mathrm{3D}}^{(1)}(\boldsymbol{r}, 0, C) > f_{\mathrm{1D}}^{(1)}(z, 0, C)$.

Hence, for the case with three-dimensional strain,

$$\begin{aligned}
S =& \int_{x,y,z} \left[\left(\frac{T - T_\eta^0}{2} \right) \eta^2 + \frac{b_z}{2} \left(\partial_z \eta \right)^2 - g_{\text{el-nem}} \eta \langle \varepsilon_{B_{1g},\mathrm{3D}} \rangle \right] \\
=& L_\parallel^2 \int_z \left[\left(\frac{T - T_\eta^0}{2} \right) \eta^2 + \frac{b_z}{2} \left(\partial_z \eta \right)^2 - \left(g_{\text{el-nem}} \frac{\frac{1}{L_\parallel^2}\int_{x,y} f_{\mathrm{3D}}(\boldsymbol{r}, \eta, C)}{f_{\mathrm{1D}}(z, \eta, C)} \right) \eta \langle \varepsilon_{B_{1g},\mathrm{1D}} \rangle \right] \\
=& L_\parallel^2 \int_z \left[\left(\frac{T - T_\eta^0}{2} \right) \eta^2 + \frac{b_z}{2} \left(\partial_z \eta \right)^2 - \left(g_{\text{el-nem}} \frac{\frac{1}{L_\parallel^2}\int_{x,y} f_{\mathrm{3D}}^{(1)}(\boldsymbol{r}, \eta, C)|_{\eta=0}}{f_{\mathrm{1D}}^{(1)}(z, \eta, C)|_{\eta=0}} \right) f_{\mathrm{1D}}^{(1)}(z, C)|_{\eta=0} \eta^2 \right],
\end{aligned} \tag{2.28}$$

where we have dropped terms higher order in η as they do not alter the nematic critical temperature due to our assumption of uniform nematicity in the plane. The corresponding expression for the purely one-dimensional system, introduced in the previous

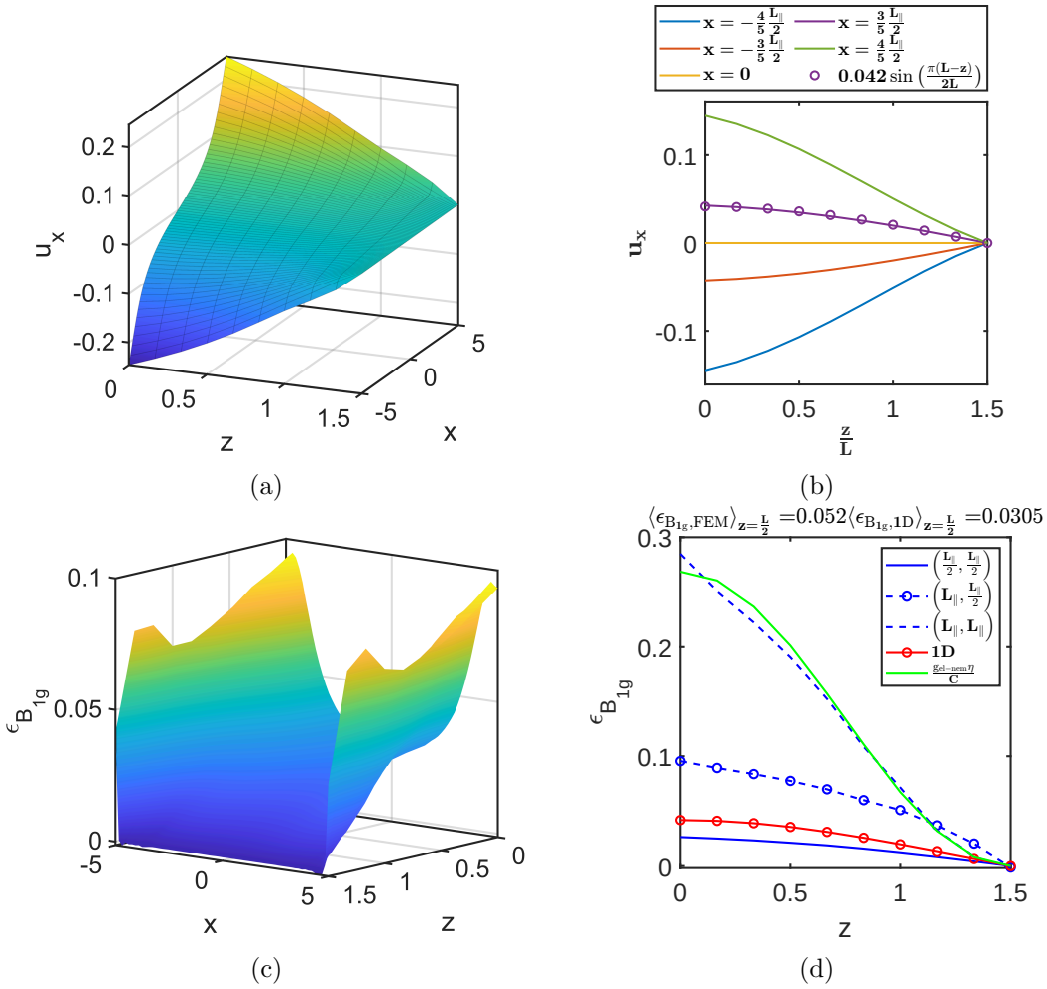

Figure 2.6: The deformation and strain profile obtained from a full three-dimensional FEM solution, with $C = 0.5$, $g_{\text{el-nem}} = \sqrt{0.1 \times C}$, and $C_{44} = 0.25$, in a sample of dimensions $10\times10\times1.5$, using an illustrative nematic field $\eta(x, y, z) = \eta_0\big[\cos(\pi z/L)+1\big]$ with $\eta_0 = 0.3$. In (a), the deformation u_x at $y = 0$ is shown while, in (b), we show cuts of panel (a) for various values of x. Also, a sinusoidal fit is plotted, which is later employed in Sec.2.4.2. In (c), we show $\varepsilon_{B_{1g}}$ at $y = 0$. In (d), along with the sections of the FEM-based strain from panel (c) (blue), we also show the corresponding result from the purely one-dimensional system with in-plane uniform strains (red), as well as the value $g_{\text{el-nem}}\eta/C$ (green), which is expected if there is no suppression from boundary constraints. The significant boundary enhancements in the FEM solution lead to a higher mean strain for each value of z as mentioned in the title, while still being smaller than $g_{\text{el-nem}}\eta/C$. Qualitatively similar results are obtained for arbitrarily small η_0.

section, is,

$$S = L_{\parallel}^2 \int_z \left[\left(\frac{T - T_\eta^0}{2} \right) \eta^2 + \frac{1}{2} b_z \left(\partial_z \eta \right)^2 - g_{\text{el-nem}} f_{\text{1D}}^{(1)}(z, C)|_{\eta=0} \eta^2 \right]. \tag{2.29}$$

Therefore, the effective nemato-elastic coupling is raised to $g_{\text{el-nem}} \frac{1}{L_{\parallel}^2} \frac{\int_{x,y} f_{\text{3D}}^{(1)}(x,y,z,\eta,C)|_{\eta=0}}{f_{\text{1D}}^{(1)}(z,\eta,C)|_{\eta=0}} \geq g_{\text{el-nem}}$, thereby raising the critical temperature.

Full three-dimensional nematicity and strain

In this section we present the full three-dimensional FEM based results for the nemato-elastic system. Since the three-dimensional nematic field can respond to the boundary enhancement of the strain, there is a mutual boundary enhancement of both fields in the self-consistent solution. As a result, the critical temperature in this case is higher than both the previously studied cases.

However, this still does *not* lead to critical temperatures greater than the standard bulk value $g_{\text{el-nem}}^2/C$, as proven earlier in Eq.(2.5) and the associated text. Alternatively, this may be seen considering the case with vanishing nematic stiffness, which would yield the highest critical temperature due to the least energy cost. In this limit, near the critical temperature where non-linearities may be neglected for simplicity, the nematic field profile mirrors that of the strain field, i.e., $\eta = g_{\text{el-nem}} \varepsilon_{B_{1g}} / (C_{11} - C_{12})$ as seen from Eq.(2.9). We formally consider a suitably normalized profile $h(x, y, z, C)$, which must otherwise be obtained from a self-consistent solution. Nevertheless, its exact form is irrelevant to our present analysis. In terms of this profile, the nematic and strain fields are written as $\eta = \eta_0 h$ and $\varepsilon_{B_{1g}} = \varepsilon_{B_{1g},0} h$, respectively. The action is now given by,

$$S = \left[\frac{T - T_\eta^0}{2} \eta_0^2 - g_{\text{el-nem}} \eta_0 \varepsilon_{B_{1g},0} + \frac{1}{2} C \varepsilon_{B_{1g},0}^2 \right] \Big(\int_{x,y,z} h^2 \Big), \tag{2.30}$$

leading to the critical temperature $g_{\text{el-nem}}^2/C$, which nothing but the result obtained in the uniform thermodynamic limit.

2.4 Approximate analytical solution

In this section, we complement the numerical results with an analytical study. We consider the two limiting cases studied above: first, the effectively one-dimensional set-up with in-plane uniformity and no boundary effects, and second, the fully three-dimensional set-up with an analytical approximation for the FEM strains.

2.4.1 One-dimensional strain and nematicity

We consider an in-plane uniform system with B_{1g} nematicity. The in-plane uniformity translates to vanishing $x, y-$derivatives of the nematic and strain fields. Defining $\varepsilon_{B_{1g}} = \frac{\varepsilon_{xx}-\varepsilon_{yy}}{\sqrt{2}} = f(z) \neq 0$, $\varepsilon_{A_{1g}} = \frac{\varepsilon_{xx}+\varepsilon_{yy}}{\sqrt{2}} = h(z)$, and $\varepsilon_{xy} = 0$, we have,

$$u_x = \frac{f(z)+h(z)}{\sqrt{2}}x, \quad u_y = \frac{-f(z)+h(z)}{\sqrt{2}}y, \tag{2.31}$$

where the A_{1g} strain, denoted by $h(z)$, corresponding to a uniform dilatation, is simply assumed to vanish in the absence of any external sources of A_{1g} symmetry. Note that this ansatz agrees with the FEM-based deformation shown in Fig.2.6(a-b). Clearly, the nematic field acts as the B_{1g} source and leads to a non-zero B_{1g} strain. Additionally, the chosen convention for the deformation fields keeps the centre of mass unchanged. Further, the absence of any forces in the $z-$ direction implies $u_z \approx 0$. Exploiting the in-plane uniformity and neglecting edge effects, $\varepsilon_{xz} = (1/\sqrt{2})(\partial_z f(z))x$, and $\varepsilon_{yz} = -(1/\sqrt{2})(\partial_z f(z))y$. An important remark regarding the validity of this approximation is in order. Recall that we have neglected boundary enhancements of the strain by assuming a constant in the plane strain and hence, a deformation profile varying linearly with x, y, as given by Eq. (2.31). Consequently, the elastic energy scales as the sample volume $\sim L_\parallel^2 L$. However, the FEM solution reveals concentrated surface strains at the $x = -L_\parallel/2, L_\parallel/2$ and $y = -L_\parallel/2, L_\parallel/2$ surfaces. As we shall show later in Eq.(2.43) and the associated text, for very thin samples, the strain is localized at the vertical faces of the sample. Considering without loss of generality the $x = L_\parallel/2$ face, the strain varies $\sim \exp(-[\ldots](L_\parallel/2-x)/L)$, where the ellipses denote a constant factor dependent on the elastic constants. Consequently, it penetrates up to a distance $x \sim L$ into the sample, instead of being uniform for $x \in [-L_\parallel/2, L_\parallel/2]$. Hence, the elastic energy

scales as $\sim L_\parallel L^2$. Therefore, for samples with larger $(L_\parallel/L)$, the non-uniform strain distribution, localized near the vertical faces of the sample, is energetically favorable. Hence, the strain is no-longer uniform and our approximation begins to fail.

Now, from Eq.(2.18), the bulk elastic action for only the deformation fields in a tetragonal system, is written as,

$$S = \int_{\boldsymbol{r}} \frac{1}{2}\Big[C_{11}(\partial_x u_x)^2 + C_{11}(\partial_y u_y)^2 + 2C_{12}(\partial_x u_x)(\partial_y u_y) + C_{44}(\partial_z u_x)^2 + C_{44}(\partial_z u_y)^2\Big]. \tag{2.32}$$

We consider an approximate solution by employing Eq.(2.31), and choosing a simple ansatz for the nematic and strain fields, $\eta_z = \eta_0 + \eta_1 \cos(\pi z/L)$ and $\varepsilon_{B_{1g}} = \varepsilon_{B_{1g},0} \sin(\pi(L-z)/2L)$. These are the lowest harmonics satisfying the boundary conditions shown in Figs.2.2 and 2.3: for the nematic field Neumann conditions at $z = 0, L$, and for the strain field zero stress at $z = 0$ and zero deformation at $z = L$. Using these profiles, the action Eq.(2.32) is written as,

$$\begin{aligned} S =& L_\parallel^2\Big[\frac{1}{2}a\eta_0^2 L + \frac{1}{2}a\eta_1^2\frac{L}{2} + \frac{1}{2}\frac{\pi^2}{2}\frac{b}{L}\eta_1^2 + \frac{1}{2}\Big(C + C_{44}\frac{L_\parallel^2}{L^2}\frac{\pi^2}{48}\Big)\frac{L}{2}\varepsilon_{B_{1g},0}^2 - g_{\text{el-nem}}\eta_0\varepsilon_{B_{1g},0}\frac{2L}{\pi} \\ & - g_{\text{el-nem}}\eta_1\varepsilon_{B_{1g},0}\frac{2L}{3\pi}\Big], \end{aligned} \tag{2.33}$$

where $a = T - T_\eta^0$. The critical temperature renormalization, a_c, is readily obtained from the functional minimization with respect to η_0, η_1, and $\varepsilon_{B_{1g},0}$, i.e., $\frac{\partial S}{\partial \eta_0} = 0$, $\frac{\partial S}{\partial \eta_1} = 0$, and $\frac{\partial S}{\partial \varepsilon_{B_{1g},0}} = 0$. Hence,

$$a_c = -\frac{b}{L^2}\frac{\pi^2}{2} + \frac{44}{9\pi^2}\frac{g_{\text{el-nem}}^2}{C_{\text{eff}}} + \frac{b}{L^2}\frac{\pi^2}{2}\left[\left(1 - \frac{88}{9\pi^4}\frac{L^2}{b}\frac{g_{\text{el-nem}}^2}{C_{\text{eff}}}\right)^2 + \frac{32}{\pi^4}\frac{L^2}{b}\frac{g_{\text{el-nem}}^2}{C_{\text{eff}}}\right]^{\frac{1}{2}} \tag{2.34}$$

$$\to \begin{cases} \frac{88}{9\pi^2}\frac{g_{\text{el-nem}}^2}{C_{\text{eff}}}, & \frac{b}{L^2} \to 0 \\ \frac{8}{\pi^2}\frac{g_{\text{el-nem}}^2}{C_{\text{eff}}}, & \frac{b}{L^2} \to \infty \end{cases}, \tag{2.35}$$

where we have defined the effectively enlarged B_{1g} elastic constant,

$$C_{\text{eff}} = C + C_{44}\frac{L_\parallel^2}{L^2}\frac{\pi^2}{48}. \tag{2.36}$$

Eq.(2.35) is shown in Fig.2.5. It is seen that the variation with b is small, ranging from $\frac{88}{9\pi^2} \approx 0.9907$ to $\frac{8}{\pi^2} \approx 0.8106$ times $g^2_{\text{el-nem}}/\big(C + C_{44}\frac{L_\parallel^2}{L^2}\frac{\pi^2}{48}\big)$, as b varies between 0 and ∞. The effect of the sample aspect ratio $L/L_\parallel$ is captured by C_{eff}, which increases as the sample is made thinner. This reflects the inevitable elastic energy cost of establishing a strain gradient, associated with the elastic constant C_{44}, corresponding to ε_{xz}, as the strain is forced to vanish at the sample-substrate interface.

2.4.2 FEM-based three-dimensional strain and three-dimensional nematicity

In this section, we derive the analytical forms of the strain and nematic fields, the scale of boundary enhancement, and the critical temperature, by using approximate expressions for the exact FEM-based three-dimensional strain field. Additionally, the results in this section allow one to rapidly obtain results without the burden of a full numerical calculation.

For simplicity, we consider a nematic field of the form

$$\begin{aligned}\eta = \eta_0 - \eta_1\big[\cos(2\pi x/L_\parallel) + \cos(2\pi y/L_\parallel)\big] - \eta_2\cos(\pi z/L)\\ + \eta_3\big[\cos(2\pi x/L_\parallel) + \cos(2\pi y/L_\parallel)\big]\cos(\pi z/L).\end{aligned} \tag{2.37}$$

This ansatz is composed of the first harmonics along all directions which satisfy the boundary conditions mentioned in Fig.2.2. This form is expected to be a good approximation when $\frac{b_\parallel}{L_\parallel^2} \gg 1$, which would penalize the higher harmonics. Additionally, the smooth Neumann boundary conditions for the nematic field helps in suppressing the sharp boundary-enhanced strain fields from drastically altering the nematic field. We do, however, retain the feedback from this nematic field to the strain problem. Now, for the elastic degrees of freedom, we approximate the $z-$dependence of the deformation field as a simple sinusoid $u_x \sim \sin\big(\frac{\pi(L-z)}{2L}\big)$, while $u_z \approx 0$ as mentioned in the previous

section. This is the lowest allowed harmonic satisfying the boundary conditions mentioned in Fig.2.3: vanishing deformation at the sample-substrate interface at $z = L$, and zero stress at the free surface $z = 0$,

$$C_{izkl}\partial_l u_k|_{z=0} = \big(C_{33}\underbrace{\partial_z u_z}_{\approx 0} + C_{13}\partial_x u_x + C_{13}\underbrace{\partial_y u_y}_{\approx -\partial_x u_x} + C_{44}\partial_z u_x + C_{44}\partial_z u_y\big)\big|_{z=0} = 0$$

$$\implies C_{44}\partial_z u_x + C_{44}\partial_z u_y|_{z=0} = 0. \tag{2.38}$$

Also, this form is motivated by Fig.2.6(b), which shows the FEM-based deformation field u_x as a function of z for a test nematic field $0.3\big[\cos(\frac{\pi(L-z)}{L}) + 1\big]$. Note that, in the absence of any $A_{1g}-$symmetric source, the $A_{1g}-$strain vanishes, implying $\partial_x u_x \approx -\partial_y u_y$. Now, using the bulk elastic equation of motion given in Fig.2.3,

$$\begin{aligned} &- \partial_j C_{ijkl}\partial_l u_k + \frac{1}{\sqrt{2}} g_{\text{el-nem}}\big[\partial_x \eta \delta_{i,x} - \partial_y \eta \delta \delta_{i,y}\big] = 0 \\ i = 1(x): \quad &- C_{11}\partial_x^2 u_x - C_{12}\partial_x \underbrace{\partial_y u_y}_{-\partial_x u_x} - C_{13}\partial_x \underbrace{\partial_z u_z}_{\approx 0} - C_{44}\partial_z^2 u_x + \frac{1}{\sqrt{2}} g_{\text{el-nem}}\partial_x \eta = 0. \end{aligned} \tag{2.39}$$

From Eq.(2.37), $\partial_x \eta = \eta_1\big(\frac{2\pi}{L_\parallel}\big)\sin\big(\frac{2\pi x}{L_\parallel}\big) - \eta_3\big(\frac{2\pi}{L_\parallel}\big)\sin\big(\frac{2\pi x}{L_\parallel}\big)\cos\big(\frac{\pi z}{L}\big)$, using which, we obtain,

$$\big(C_{11} - C_{12}\big)\partial_x^2 u_x - C_{44}\Big(\frac{\pi}{2L}\Big)^2 u_x = \frac{g_{\text{el-nem}}}{\sqrt{2}}\frac{2\pi}{L_\parallel}\sin\Big(\frac{2\pi x}{L_\parallel}\Big)\Big[\eta_1 - \eta_3\cos\Big(\frac{\pi(L-z)}{L}\Big)\Big]. \tag{2.40}$$

This yields an exponentially decaying "homogeneous" solution for u_x along the $x-$direction, along with an "inhomogeneous" sinusoidal response to the nematic field. The corresponding expression for u_y is readily obtained by changing $x \leftrightarrow y$, and flipping the sign of the nemato-elastic term, as it appears with an extra minus sign in the

corresponding bulk equation for the $y-$component. Hence, the strains are obtained as,

$$\varepsilon_{B_{1g}} = \varepsilon_{B_{1g},0}\upsilon_1 \cos\left(\frac{\pi z}{2L}\right) + \upsilon_2 \frac{16\frac{g_{\text{el-nem}}}{(C_{11}-C_{12})}\left[\eta_1 + \eta_3 \cos\left(\frac{\pi z}{L}\right)\right]}{\frac{C_{44}}{(C_{11}-C_{12})}\left(\frac{L_\parallel}{L}\right)^2 + 16}, \tag{2.41a}$$

$$\varepsilon_{xz} = \frac{-\sqrt{2}\varepsilon_{B_{1g},0}}{\sqrt{\frac{C_{44}}{C_{11}-C_{12}}}}\upsilon_3 \sin\left(\frac{\pi z}{2L}\right) + \frac{4\sqrt{2}\frac{g_{\text{el-nem}}}{(C_{11}-C_{12})}\left(\frac{L_\parallel}{L}\right)\sin\left(\frac{2\pi x}{L_\parallel}\right)\left[\eta_3 \sin\left(\frac{\pi z}{L}\right)\right]}{\frac{C_{44}}{(C_{11}-C_{12})}\left(\frac{L_\parallel}{L}\right)^2 + 16}, \tag{2.41b}$$

where,

$$\upsilon_1 = \cosh\left(\frac{\pi x}{2L}\sqrt{\frac{C_{44}}{C_{11}-C_{12}}}\right) + \cosh\left(\frac{\pi y}{2L}\sqrt{\frac{C_{44}}{C_{11}-C_{12}}}\right), \tag{2.42a}$$

$$\upsilon_2 = \cos\left(\frac{2\pi x}{L_\parallel}\right) + \cos\left(\frac{2\pi y}{L_\parallel}\right), \tag{2.42b}$$

$$\upsilon_3 = \sinh\left(\frac{\pi x}{2L}\sqrt{\frac{C_{44}}{C_{11}-C_{12}}}\right). \tag{2.42c}$$

This defines the boundary enhancement scale,

$$\xi_\parallel = \left[\frac{\pi}{2L}\sqrt{\frac{C_{44}}{C_{11}-C_{12}}}\right]^{-1}, \tag{2.43}$$

governing the depth over which the boundary enhancement effects in the strain field profiles propagate into the bulk of the sample. Importantly, $\xi_\parallel$ is small for thin samples with $L \ll L_\parallel$, suggesting that the strains primarily develop and relax close to the vertical faces of the sample, with the bulk remaining relatively unstrained. This is a consequence of the Dirichlet condition at the sample-substrate interface, as a result of which, any bulk strain is forced to rapidly relax to zero at the interface, incurring a large elastic gradient energy cost. Note that this procedure does not exactly replicate the results of the FEM simulation. Instead, near the critical temperature when the nematic fields are small, and for large nematic stiffness when the higher nematic harmonics are even smaller, we obtain the qualitative spatial features. Instead of determining the coefficient $\varepsilon_{B_{1g},0}$ at this point, which would require an otherwise uncontrolled approximation, we solve for it variationally.

Now, to get the values of the order parameters $\eta_0 \ldots \eta_3$ and $\varepsilon_{B_{1g},0}$, we consider the Gaussian action derived from Eq.(2.32), $S = \iiint dxdydz\left[\frac{1}{2}a\eta^2 + \frac{1}{2}b_\parallel|\nabla_\parallel\eta|^2 + \frac{1}{2}b(\partial_z\eta)^2 -\right.$

$g_{\text{el-nem}}\eta\varepsilon_{B_{1g}} + \frac{1}{2}C_{B_{1g}}\varepsilon^2_{B_{1g}} + 2\times\frac{1}{2}C_{44}\varepsilon^2_{xz}\big]$. Here, the factor of two multiplying the strain energy corresponding to ε_{xz} is due to the two degenerate contributions from $\int\varepsilon^2_{xz} = \int\varepsilon^2_{yz}$, which is obtained by using the prescription relating u_y to u_x mentioned earlier. Subsequently, we substitute the expressions derived above for the nematic and strain fields, and perform the spatial integrations. We introduce the following integrals, $I_1 = \frac{1}{L_\parallel^2}\iint_{x,y}\upsilon_1$, $I_2 = \frac{1}{L_\parallel^2}\iint_{x,y}\upsilon_1^2$, $I_3 = \frac{1}{L_\parallel^2}\iint_{x,y}\upsilon_3^2$, $I_4 = \frac{1}{L_\parallel^2}\iint_{x,y}\upsilon_1(x,y)(-\upsilon_2)$, and $I_5 = \frac{1}{L_\parallel^2}\iint_{x,y}\upsilon_3\sin\left(\frac{2\pi x}{L_\parallel}\right)$, which arise from the in-plane spatial integrations of the field profiles. The resulting lengthy yet straightforward expressions are omitted for brevity, and later directly state the relevant limiting values. We rewrite the spatially-integrated action as,

$$S = L_\parallel^2 L\Bigg[\sum_{j=0}^{3}\frac{1}{2}a_j\eta_j^2 + \frac{1}{4}(C_{11}-C_{12})[I_2+4I_3]\varepsilon^2_{B_{1g},0} - \sum_{j=0}^{3}g_{\text{el-nem},j}\eta_j\varepsilon_{B_{1g},0}\Bigg], \tag{2.44}$$

where the nemato-elastic couplings $g_{\text{el-nem},0\ldots3}$ for the nematic fields are functions of $I_{1\ldots5}$ and the sample dimensions $L, L_\parallel$. Once again, we omit the lengthy expressions for these couplings for brevity. On integrating out the strain field,

$$S = L_\parallel^2 L\Bigg[\frac{1}{2}\sum_{j=0}a_j\eta_j^2 - \frac{1}{2}\frac{2\big(\sum_{j=0}^{3}g_{\text{el-nem},j}\eta_j\big)^2}{\big(C_{11}-C_{12}\big)[I_2+4I_3]}\Bigg] \tag{2.45}$$

The saddle-point equations are obtained as,

$$\frac{\partial S}{\partial\eta_j} = \Bigg[a_j - 2\frac{\frac{g^2_{\text{el-nem},j}}{(C_{11}-C_{12})}}{[I_2+4I_3]}\Bigg]\eta_j - \sum_{k\neq j}\Bigg[2\frac{\frac{g_{\text{el-nem},j}g_{\text{el-nem},k}}{(C_{11}-C_{12})}}{[I_2+4I_3]}\Bigg]\eta_k = 0. \tag{2.46}$$

The numerical solution of Eq.(2.46) is shown in Fig.2.7. As mentioned earlier, the critical temperature is capped by the corresponding bulk value $g^2_{\text{el-nem}}/C$. This is approached in the limit $L/L_\parallel \to \infty$ when $\xi_\parallel/L_\parallel \to \infty$ and as such, the in-plane inhomogeneities vanish. Further, as expected, the critical temperature decreases with increasing stiffness $b, b_\parallel$.

Now, in the $b/L^2 \to \infty$ limit, $\eta_2 = \eta_3 = 0$ as the $z-$ variation is suppressed. The corresponding strains are obtained from Eq.(2.41) by setting η_3 to zero. On substituting

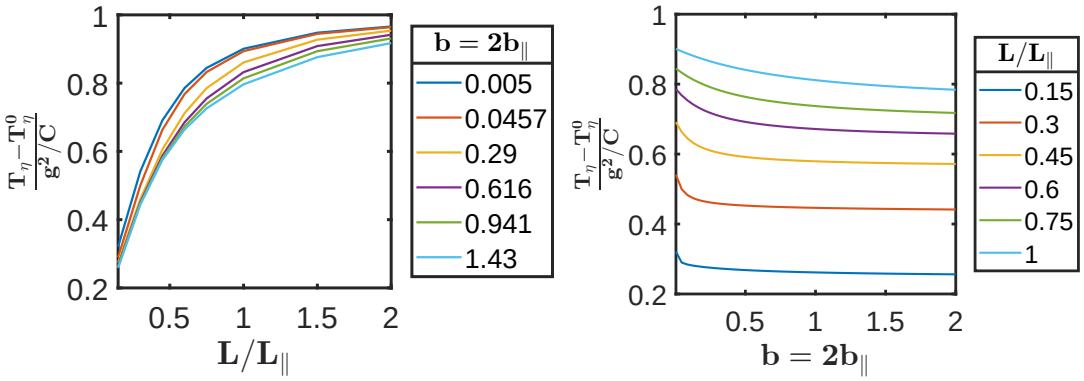

(a) (b)

Figure 2.7: The nematic critical temperature T_η obtained from Eq.(2.46), as a function of (a) the aspect ratio $L/L_\parallel$, and (b) the stiffness $b = 2b_\parallel$, for $C = 0.5$, $C_{44} = 0.05$ and $g_{\text{el-nem}} = \sqrt{0.1C}$. As seen from (a), that the critical temperature reaches the bulk value in the $L/L_\parallel \to \infty$ limit.

these into the Gaussian action, we obtain,

$$S = L_\parallel^2 L\left[\frac{1}{2}a_0\eta_0^2 + \frac{1}{2}a_1\eta_1^2 - \frac{(g_{\text{el-nem},0}\eta_0 + g_{\text{el-nem},1}\eta_1)^2}{2\frac{(C_{11}-C_{12})}{2}\big[I_2 + 4I_3\big]}\right]. \tag{2.47}$$

The corresponding saddle-point equations are readily obtained as,

$$\frac{\partial S}{\partial \eta_0} = \left[a_0 - \frac{g_{\text{el-nem},0}^2}{(C_{11}-C_{12})}\frac{2I_1^2}{\big[I_2+4I_3\big]}\right]\eta_0 - \frac{g_{\text{el-nem},0}g_{\text{el-nem},0}}{(C_{11}-C_{12})}\frac{\frac{8}{\pi^2}I_1I_4}{\big[I_2+4I_3\big]}\eta_1 = 0, \tag{2.48a}$$

$$\frac{\partial S}{\partial \eta_1} = -\frac{g_{\text{el-nem},0}g_{\text{el-nem},0}}{(C_{11}-C_{12})}\frac{\frac{8}{\pi^2}I_1I_4}{\big[I_2+4I_3\big]}\eta_0 + \left[a_1 - \frac{g_{\text{el-nem},1}^2}{(C_{11}-C_{12})}\frac{2I_1^2}{\big[I_2+4I_3\big]}\right]\eta_1 = 0, \tag{2.48b}$$

which yields the renormalized critical temperature, T_η. An analytical approximation may be obtained in the limit $b_\parallel/L_\parallel^2 \gg 1$. Now, motivated by the presence of the boundary enhancement scale derived earlier in Eq.(2.43), we focus on the two-limiting cases of relevance to clearly highlight the effects of the sample dimensions. First, we consider a thin sample with $L/L_\parallel \to 0$ where $\xi_\parallel \to 0$ and thus the boundary effects are dominant with the strain primarily developing only at the vertical surface of the sample. In this case, we have $I_1 = I_4 \approx \frac{8}{\pi}\frac{L}{L_\parallel}\sqrt{\frac{C_{11}-C_{12}}{C_{44}}}\exp\big(\frac{\pi L_\parallel}{4L}\sqrt{\frac{C_{44}}{C_{11}-C_{12}}}\big)$ and $I_2 =$

$2I_3 \approx \frac{2}{\pi}\frac{L}{L_\parallel}\sqrt{\frac{C_{11}-C_{12}}{C_{44}}}\exp\left(\frac{\pi L_\parallel}{2L}\sqrt{\frac{C_{44}}{C_{11}-C_{12}}}\right)$. Hence, we have,

$$\eta_0 = \frac{\eta_1}{}\sqrt{\frac{T_\eta^R - T}{u_\eta}}\Theta(T_\eta^R - T), \tag{2.49a}$$

$$\eta_1 = \frac{1}{4\pi^2}\frac{L_\parallel^2}{b_\parallel}\frac{g_{\text{el-nem}}^2}{C}\left(\frac{256}{3\pi^3}\sqrt{\frac{C}{C_{44}}}\right)\frac{L}{L_\parallel}\sqrt{\frac{T_\eta^R - T}{u_\eta}}\Theta(T_\eta^R - T), \tag{2.49b}$$

with the renormalised critical temperature T_η is given by,

$$(T_\eta - T_\eta^0)\Big|_{\frac{b}{L^2}\to\infty}^{\frac{L}{L_\parallel}\to 0} = \frac{g_{\text{el-nem}}^2}{C}\left(\frac{256}{3\pi^3}\sqrt{\frac{C}{C_{44}}}\right)\frac{L}{L_\parallel} + \frac{1}{4\pi^2}\left[\frac{g_{\text{el-nem}}^2}{C}\left(\frac{256}{3\pi^3}\sqrt{\frac{C}{C_{44}}}\right)\frac{L}{L_\parallel}\right]^2\frac{L_\parallel^2}{b_\parallel}, \tag{2.50}$$

where $C = C_{11} - C_{12}$. The critical temperature is found to decrease linearly with the aspect ratio $L/L_\parallel \to 0$ at the leading order for thin samples. This is a consequence of the Dirichlet condition at the sample-substrate interface and the associated shear elastic energy cost to establish a bulk strain in thin samples. Second, in the opposite limit, $L/L_\parallel \to \infty$, the boundary enhancement scale diverges $\xi_\parallel \to \infty$ and hence, the strain field is uniform in the plane. Additionally, the effects of the clamping at the sample-substrate interface is expected to vanish. In this case, we obtain, $I_1 = \frac{I_2}{2} \approx 2$, and $I_3 = I_4 \approx 0$, thereby yielding,

$$(T_\eta - T_\eta^0)\Big|_{\frac{b}{L^2}\to\infty}^{\frac{L}{L_\parallel}\to\infty} = \frac{g_{\text{el-nem}}^2}{C}\frac{8}{\pi^2}. \tag{2.51}$$

Thus, the lattice renormalized critical temperature attains a value close to, but still smaller than the corresponding bulk result $g_{\text{el-nem}}^2/(C_{11} - C_{12})$. Note that this result is the same as the one obtained in Eq.(2.35) in the $b/L^2 \to \infty$ limit, where we neglected the boundary effects by considering a system with in-plane uniformity.

2.5 Conclusion

To summarize, we have shown that in finite-size samples glued to a substrate, the nematic and strain fields are in general inhomogeneous. We have obtained a boundary

enhancement scale $\xi_{\|}$ in Eq.(2.43), which is a measure of the distance over which boundary effects near the vertical faces of the sample propagate into the bulk. As a result, for thin samples, the strain develops only near the vertical faces of the sample, vanishing exponentially into the bulk of the sample. Physically, this is a consequence of the Dirichlet condition on the deformation fields at the sample substrate interface, which causes bulk strain fields to be accompanied by an elastic gradient energy corresponding to the shear strains. While one might expect the non-linear boundary enhancements to enhance the overall response of the lattice to the electronic nematicity, our theoretical results show that this is not the case. Importantly, as the sample is made thinner, the nematic critical temperature *decreases* due to the elastic gradient energy cost, scaling as the sample dimensional aspect ratio $L/L_{\|}$ at the leading order.

On the one hand, these results open up avenues to experimentally study finite-size effects on the nematic critical temperature in epitaxially grown single crystals of varying thickness. Such samples, devoid of dislocations and other lattice defects/imperfections at which the strain can otherwise relax, would allow the inhomogeneous strain fields to establish freely and reveal the interplay with nematicity and test our predictions. On the theoretical side, better and controlled analytical approximations to the finite-element-method based numerical solution may be constructed to obtain a quantitative match, as well as reveal the intricate role of the physical parameters in influencing the observed behavior.

On the other hand, noting that most experiments (see for instance Refs. [54, 38, 71]) typically use samples with $L/L_{\|} \in (1/30, 1/2)$, these results are intriguing in light of the possible signatures of supercritical nematicity. In fact, for the typical sample dimensions employed in experiments, a significant decrease is expected, of the order of the bulk critical temperature renormalization due to the lattice. As such, it emphasizes the existence of other mechanisms which could explain the observed supercritical nematicity.

Chapter 3

Surface elastic defects and smecticity

3.1 Introduction

Disorder is an inevitable part of any electronic system, which can significantly impact the electronic properties in both negative as well as non-trivially positive ways. In particular, a number of studies have theoretically [58, 50, 51] and experimentally [59, 41, 60, 61, 62, 49] considered the impact of disorder on nematicity as well as superconductivity in FeSCs. Interestingly, some of these studies have suggested super-critical nematic order from anisotropic defects [49, 47], and residual strain [41, 72, 52].

Motivated by the large nemato-elastic coupling [7, 30, 31, 32, 33, 34, 35, 36], and the possibility of supercritical nematicity at the surface, we consider the effect of a specific class of random defects on the surface. The surface morphology of a crystal is the result of complex interactions between the atoms, environment, as well as the sample growth and preparation conditions, which in turn can have significant ramifications for the thermodynamic and electronic properties. One class of defects on an idealised crystal surface usually consists of terrace domains separated by parallelly aligned steps of varying heights, as well as point defects such as kinks and adatoms which may generically be anisotropic, i.e., C_2-symmetric. In our study, for definitiveness, we consider domains of step defects of random strengths on the exposed surface of the sample, which are often naturally present. In fact, cleaving a crystal surface constitutes an explicit

breaking of the surface rotation symmetry and as such, domains of anisotropic defects are not surprising. We show that such a domain of parallelly aligned anisotropic defects indeed leads to a macroscopic supercritical transition to a modulated nematic, i.e., a smectic state. While the spotlight has primarily been on the uniform nematic state in both FeSCs as well as the cuprates, some studies have previously investigated electronic smecticity in these systems both theoretically [73, 74, 75, 76, 77, 78, 79, 80], and experimentally [81, 82, 83]. The theoretical studies, which have only considered the cuprates, have largely explored either a finite $\boldsymbol{q}$ charge nematic instability, with the $\boldsymbol{q}$ determined by position of the Fermi level relative to van Hove singularities on a square lattice, or a sub-leading instability (to spin density wave order) mediated by antiferromagnetic spin fluctuations. On the other hand, the experimental studies deal with STM observations of smectic stripes in FeSe thin films, adding to its list of intriguing properties. Importantly, the experimental observations reveal incommensurate smecticity, with the ordering wavevector seemingly independent of the FeSe film-thickness and the Fermi-surface topology.

In this work, in a complementary approach to the ones introduced above, we show that suitable random elastic defects can lead to a supercritical incommensurate smectic state. Indeed experiments have indicated the critical role of elastic defects in inducing smecticity [81, 82, 83]. As a tractable proof of concept, we restrict ourselves to the simple model of anisotropic defects, namely, step defects, which nevertheless embody the generic elastic features leading to smecticity. Our primary results are as follows: Employing a phenomenological Ginzburg-Landau free energy functional for the nematic fields, along with a simple description of the defects using linear elasticity, we obtain a disorder induced non-local nematic potential by averaging over the defect realizations. Remarkably, on minimizing this renormalized nematic action, a finite $\boldsymbol{q}$ supercritical nematic state is obtained, with the wavevector $\boldsymbol{q}$ determined solely by the elastic constants of the material and the nematic Ginzburg-Landau parameters. Finally, the disorder-renormalized nematic action is numerically solved to present a physical picture of the smectic state, demonstrating the supercritical smectic state which gradually transitions into the uniform disordered bulk over the nematic critical temperature, and the uniform nematic state below it.

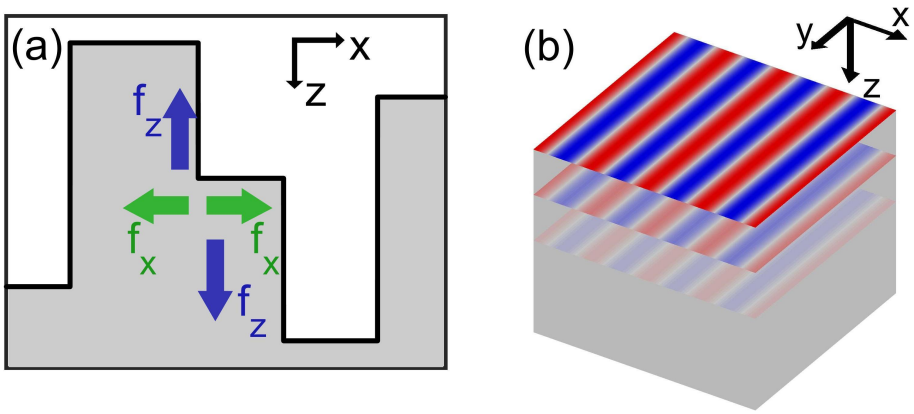

Figure 3.1: (a) A section of the sample, showing parallelly aligned steps of random heights/strengths on the surface, with the steps being infinite in length, oriented parallel to the $y-$ axis, and changing in height along the $x-$axis. The forces generated by a single step are marked. (b) An illustration of the supercritical surface smecticity, shown here as a modulated nematic field, decaying into the bulk of the sample to zero.

3.2 Surface step disorder

3.2.1 Model

We consider an isotropic elastic half-space ($z \leq 0$) for simplicity, with E and ν being the Young′s modulus and Poisson′s ratio, respectively. The exposed surface has a distribution of elastic defects which, in general, are anisotropic in shape. In the standard approach, the deformation field of a defect is calculated by replacing it by a distribution of localized forces acting on the underlying semi-infinite crystal [84, 85, 86, 87, 88, 89, 90], which may be conveniently specified in terms of its elastic multipole moments. Since the system is in equilibrium, the resultant force and net moment vanish and hence, far from the source, the dipolar term survives at the leading order. For simplicity, we restrict ourselves to the idealised case of infinite step defects, which are essentially infinitely long anisotropic defects, with each step defect being as shown in Fig.3.1(b). As such, it encapsulates the fundamental principle crucial to our work while being amenable to a tractable analytical analysis. We focus on a domain of steps distributed parallel to the $y-$axis, and having random strengths and locations. A single step located at $x = x'$ is modeled by the force $f_j = A_j \partial_x \delta(x - x')$, where $j = 1, 3$ denote the $x-$ and $z-$

components, and A_j characterizes the strength of the defect. The dipolar form of this force, illustrated in Fig.3.1(b), is crucial to the results to follow. Subsequently, using the Green's function for an infinite line-force along the $y-$ axis in a half-space [91], $G_{xz} = \frac{(1-\nu^2)}{\pi E}[(1 - \frac{\nu}{1-\nu})\sin^{-1}\frac{x}{r} + (1 + \frac{\nu}{1-\nu})\frac{xz}{r^2}]$, with $r = \sqrt{x^2+z^2}$, the deformation created by a single step located at $(x, z) = (x', 0)$ is given by,

$$u_i = \int_{x''} G_{ij}(x - x'', z - 0)A_j\partial_{x''}\delta(x'' - x') = A_j\partial_x G_{ij}(x - x', z), \tag{3.1}$$

For simplicity, we restrict ourselves to only the $z-$component of the force, i.e., $A_1 = 0$ but $A_3 \neq 0$. The strains, for a defect located at $x = x'$, are therefore given by,

$$\varepsilon_{xx} = -A_3\frac{4(1+v)}{\pi E}\left[\frac{(\nu-1)(x-x')^3 z + (\nu+1)(x-x')z^3}{\left((x-x')^2+z^2\right)^3}\right] \tag{3.2a}$$

$$\xrightarrow[\text{transforming}]{\text{Fourier}} \frac{(1+\nu)A_3}{EL_\parallel}\text{sign}(z)\sum_{q_x} iq_x[|q_x||z| + 2\nu - 1]e^{-|q_x||z|}e^{iq_x(x-x')}, \tag{3.2b}$$

along with $\varepsilon_{yy} = 0$. Consequently, there is a B_{1g} strain, $(\varepsilon_{xx} - \varepsilon_{yy})/\sqrt{2}$, which promotes nematic order. Note that the uniform $\boldsymbol{q}_\parallel = 0$ component of the strain vanishes, which is crucial for the results to follow. This feature is rather generic to all defects in equilibrium. As mentioned earlier, the case of step defects permits a simple closed-form solution.

3.2.2 Step-disorder renormalised nematic potential

Here we obtain the renormalized nematic potential by performing a disorder averaging over a domain of parallelly aligned steps with random strengths. Before proceeding, we take a moment to comment on the formalism. Disorder averaging is broadly classified into two categories depending on the kind of disorder and their associated dynamics, namely, quenched and annealed averaging. In the case of quenched averages, the disorder is considered conformationally and dynamically static, at least in the time-scale of the relevant experimental measurement. In contrast, in the case of annealed averages, the disorder source responds to the dynamical fields, and is therefore in thermal equilibrium. A generic observable is calculated as $\langle O\rangle = \partial^n \ln(Z)/\partial J_1\partial J_2\ldots\partial J_n|_{\boldsymbol{J}=0} = (1/Z)(\partial^n Z/\partial J_1\partial J_2\ldots\partial J_n|_{\boldsymbol{J}=0})$, where the vector of artificial $\boldsymbol{J}$ sources generate the

observable O. The formal implementation of annealed averages is technically much simpler as the disorder sources are treated on an equal footing with the dynamical fields while calculating the partition function. However, in the case of quenched averages, the averaging is performed at the end, after already calculating the required quantity. Using $\langle \bar{O} \rangle = \int P(V)(1/Z)(\partial^n Z/\partial J_1 \partial J_2 \dots \partial J_n)$, where Z depends on the specific instance of the disorder potential V, with the associated probability density being given by $P(V)$, it is clear that the denominator $1/Z$ is the biggest issue, as the subsequent integral over disorder realizations is rendered analytically impossible. To circumvent this issue, an exact treatment of the random *quenched* defects is typically performed using either the replica trick, Keldysh formalism, or the supersymmetric approach. In the replica field-theoretic approach, where the extensive self-averaging quantity $\ln(Z)$ is averaged over the disorder configurations, one exploits the formal relation $\ln(Z) = \lim_{n\to 0}(Z^n - 1)/n$, which eliminates the denominator entirely. In this work we use the simpler *annealed* average, as the replica trick is primarily useful only when there is replica symmetry breaking and/or replica fluctuations associated with metastability. For a disorder characterized by a coupling g and disorder source standard deviation $\sqrt{h^2}$, which in our case represent the nemato-elastic coupling and the variance of the random strain fields, the disorder potential energy valleys have heights $\sim g\sqrt{h^2}$. Since our range of temperatures $T \sim g^2_{\text{el-nem}}/C \sim 50 - 130K$ is already a sufficiently large scale, we have $T \sim g^2_{\text{el-nem}}/C > g\sqrt{h^2}$ for sufficiently small disorder strength and hence, we expect the replica symmetric solution to hold well, which is the same as the much simpler annealed averaging.

Now, we consider a domain with a distribution of steps aligned parallel to each other along the $y-$axis, as a parallel arrangement is energetically favorable. Each step, indexed by j, has a random strength $h_j = (1+\nu)A_{3,j}/(\sqrt{2}E)$ satisfying $\langle h_j h_{j'} \rangle = \bar{\sigma}^2 \delta_{j,j'}$. Hence, the net strain created by the distribution of steps can be written as, $\varepsilon_{B_{1g},\boldsymbol{r}} = \sum_j h_j \varepsilon_{B_{1g},\boldsymbol{r}-\boldsymbol{r}_j}$. We define a dimensionless continuous defect strength field, $\rho_x = \int_{y=x-L_\xi/2}^{x+L_\xi/2} \sum_j h_j \delta_{y-x_j}$, where δ_x is the Dirac delta function, and L_ξ is ideally much larger than the spacing between the steps, but much smaller than the bare nematic correlation length. As such, the following analysis is good for temperatures close to the

bare nematic critical temperature. The continuous defect strength field satisfies,

$$\langle \rho_x \rho_x \rangle = \sum_{j,j'} \int_{x-L_\xi/2}^{x+L_\xi/2} dy \int_{x-L_\xi/2}^{x+L_\xi/2} dy' \langle h_j h_{j'} \rangle \delta_{y-x_j} \delta_{y'-x_{j'}} = \sum_j \sigma^2 = \bar{\sigma}^2 n_{\text{step}} L_\xi, \quad (3.3)$$

where $n_{\text{step}} = \frac{N_{\text{step}}}{L_\parallel}$ is the step concentration. This yields the Gaussian probability

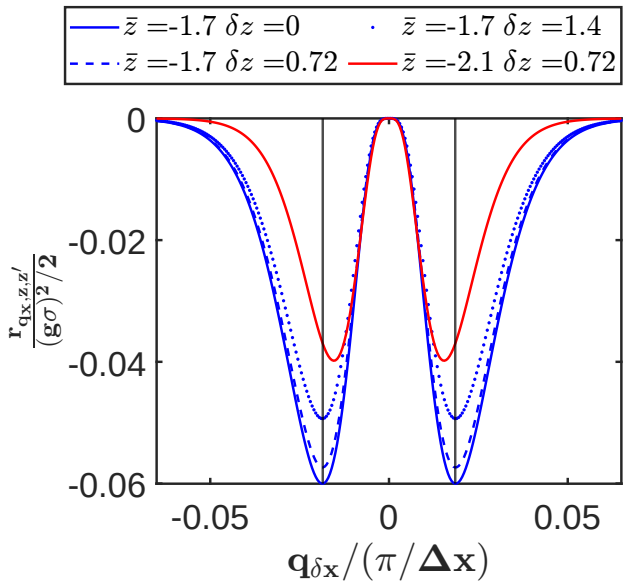

Figure 3.2: The nematic potential in momentum space, showing troughs at $q_{\max} \sim \frac{1}{|\bar{z}|}$, where $\bar{z} = (z + z')/2$ is the mean depth.

measure for the step strength, $P_\rho = \exp(-\sum_j \frac{h_j^2}{2\sigma'^2}) = \exp(-\frac{1}{L_\parallel}\int_x \frac{\rho_x^2}{2\sigma^2})$, where we have defined $\sigma^2 = \bar{\sigma}^2 \frac{n_{\text{step}} L_\xi}{N_\parallel} = \bar{\sigma}^2 \frac{N_{\text{step}}}{N_\parallel} \frac{L_\xi}{L_\parallel}$. Hence, the partition function is obtained as,

$$\begin{aligned}
\mathcal{Z} &= \int_{\eta,\rho} \exp\left[-\int_{\boldsymbol{r}} \eta_{\boldsymbol{r}_\parallel,z} \frac{a - b_\parallel \nabla_\parallel^2 - b\partial_z^2}{2} \eta_{\boldsymbol{r}_\parallel,z} + \frac{g}{L_\parallel} \int_{\boldsymbol{r},x''} \rho_{x''} \varepsilon_{\boldsymbol{r}_\parallel - x''_\parallel,z} \eta_{\boldsymbol{r}_\parallel,z} \right] P_\rho, \\
&= \int_\eta \exp\left[-\int_{\boldsymbol{r}} \eta_{\boldsymbol{r}_\parallel,z} \frac{a - b_\parallel \nabla_\parallel^2 - b\partial_z^2}{2} \eta_{\boldsymbol{r}_\parallel,z} + \frac{(g\sigma)^2}{2L_\parallel} \int_{\boldsymbol{r},\boldsymbol{r}',x''} \varepsilon_{\boldsymbol{r}-x'',z} \varepsilon_{\boldsymbol{r}'-x'',z'} \eta_{\boldsymbol{r}_\parallel,z} \eta_{\boldsymbol{r}'_\parallel,z'} \right], \\
&= \int_\eta \exp\left[-\sum_{\boldsymbol{q}_\parallel} \int_z \eta_{-\boldsymbol{q}_\parallel,z} \frac{a + b_\parallel \boldsymbol{q}_\parallel^2 - b\partial_z^2}{2} \eta_{\boldsymbol{q}_\parallel,z} - \int_{z,z'} \sum_{q_x} \underbrace{\frac{-(g\sigma)^2}{2} \varepsilon_{-q_x,z} \varepsilon_{q_x,z'}}_{r_{q_x,z,z'}} \eta_{q_x,z} \eta_{-q_x,z'} \right],
\end{aligned} \quad (3.4)$$

where, we have used $\eta_{\boldsymbol{r}_\parallel,z} = \frac{1}{(L_\parallel^{1/2})^2}\sum_{\boldsymbol{q}_\parallel}\eta_{\boldsymbol{q}_\parallel,z}e^{i\boldsymbol{q}_\parallel\cdot\boldsymbol{r}_\parallel}$, and an analogous expression for ε, with the normalization $1/\sqrt{L_\parallel}$ for each coordinate. Using Eq.(3.2), the disorder generated non-local potential term is written as,

$$r_{q_x,z,z'} = -\frac{(g\sigma)^2}{2}q_x^2[|q_x||z| + 2\nu - 1][|q_x|z' + 2\nu - 1]e^{-|q_x|(|z|+|z'|)}. \tag{3.5}$$

Note that $r_{q_x,z,z'}$ is peaked at a non-zero value of q_x, and vanishes at $q_x = 0$, which is, crucially, a consequence of the dipolar structure of the strain. This is shown in Fig.3.2.

3.2.3 Critical temperature

Exact calculation

Beginning with the action,

$$S = \sum_{\boldsymbol{q}_\parallel}\int_{z\leq 0}\frac{1}{2}\left[\left(\frac{T - T_\eta^0}{T_\eta^0} + b_\parallel q_x^2\right)|\eta_{z,\boldsymbol{q}_\parallel}|^2 + b|\partial_z\eta_{z,\boldsymbol{q}_\parallel}|^2\right] + \int_{z,z'\leq 0} r_{q_x,z,z'}\eta^*_{z,q_x}\eta_{z',q_x}, \tag{3.6}$$

we Fourier transform along the $z-$direction using the basis

$$\eta_{q_x,z} = \eta_{q_x,m}\big[\delta_{m,0} + \sqrt{2}\cos\big(\frac{m\pi}{L}\big)(1 - \delta_{m,0})\big], \tag{3.7}$$

in a regularized sample of $z-$thickness L. We omit the lengthy expression for the action in this basis, which is otherwise trivial to obtain. The saddle-point equation is readily solved by considering a sufficiently large finite number of modes $m \leq m_{\max}$, and searching for the value of $(T - T_\eta^0)/T_\eta^0 = (T_\eta - T_\eta^0)/T_\eta^0$ where the condition number[1] of matrix representing the saddle-point equation diverges. The results are presented in Fig.3.3. showing that the critical temperature is peaked at a finite q_x. This peak is obtained due to the nematic gradient energy costs eventually suppressing the critical temperature for large q_x.

[1]Ratio of the largest and the smallest eigenvalue. A matrix with a large condition number is nearly singular.

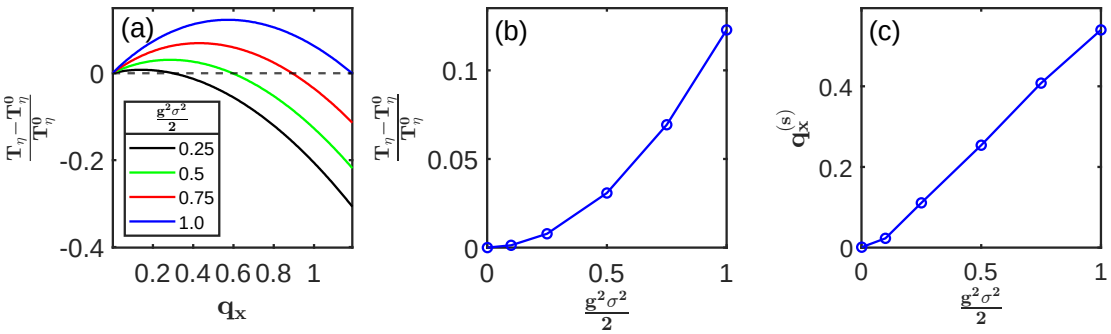

Figure 3.3: The critical temperature for $L \to \infty$, $b = 0.5 = 2b_{\|}$, and $\nu = 0.495$. (a) The variation of the critical temperature with the q_x. The eventual quadratic decrease with increasing q_x is a consequence of the gradient energy. (b) The actual critical temperature (peak value in the left panel) is found to vary quadratically with the effective defect strength $\frac{g^2\sigma^2}{2}$. (c) The smectic wavevector $q_x^{(s)}$ as a function of the effective defect strength $(g\sigma)^2/2$, found to increase approximately linearly.

Analytical approximation

Now, we obtain an analytical approximation for the critical temperature. As a simplifying approximation, we neglect the stiffness along the $z-$direction, $b(\partial_z \eta)^2$, which is reasonable as the iron superconductors have relatively much larger inter-layer spacing compared to the intra-layer lattice constants. In this approximation, the boundary conditions along the $z-$direction, mentioned in Fig.2.2, are no longer required. This drastically simplifies the saddle-point equation to,

$$\left(\frac{T - T_\eta^0}{T_\eta^0} + b_{\|} q_x^2\right) \eta_{z,\boldsymbol{q}_{\|}} - (g\sigma)^2 q_x [|q_x||z| + 2\nu - 1] e^{-|q_x||z|} R = 0. \tag{3.8}$$

where we have defined $R = \int_{-\infty}^{0} dz' |q_x| [|q_x||z'| + 2\nu - 1] e^{-|q_x||z'|} \eta_{z',\boldsymbol{q}_{\|}}$. Hence,

$$\eta_{z,q_x} = (g\sigma)^2 \frac{q_x [|q_x||z| + 2\nu - 1] e^{-|q_x||z|} R}{\left(\frac{T - T_\eta^0}{T_\eta^0} + b_{\|} q_x^2\right)}. \tag{3.9}$$

Finally, the critical temperature as a function of the wavevector, $a_c(q_x)$, is obtained by imposing the self-consistency condition $R = \int_{-\infty}^{0} dz'|q_x|[|q_x||z'| + 2\nu - 1]e^{-|q_x||z'|}\eta_{z',\boldsymbol{q}_\parallel}$,

$$\frac{T_\eta(q_x) - T_\eta^0}{T_\eta^0} = (g\sigma)^2|q_x|\left(\frac{1}{4} - \nu(1-2\nu)\right) - b_\parallel q_x^2. \tag{3.10}$$

In the absence of any electronic phase-space constraints, this leads to the wavevector $q_x^{(s)} = \frac{(g\sigma)^2}{4b_\parallel}\left(\frac{1}{4} - \nu(1-2\nu)\right)$, which orders first, leading to incommensurate smecticity with $q_x^{(s)}$ dependent only on the elastic constants and the nematic free energy parameters. The corresponding reduced critical temperature is obtained by evaluating $(T_\eta(q_x^{(s)}) - T_\eta^0)/T_\eta^0$, yielding,

$$\frac{T_\eta(q_x^{(s)}) - T_\eta^0}{T_\eta^0} = (g\sigma)^4\left(\frac{1}{4} - \nu(1-2\nu)\right)^2 \frac{1}{4b_\parallel}. \tag{3.11}$$

Further, from the profile of the nematic field, as seen from Eq. (3.9), it is found that $\eta_{z,\boldsymbol{q}_\parallel}$ is peaked at $z \sim 1/q_x$ and exponentially decays into the bulk. In spite of what Eq.(3.10) might suggest, in the presence of the nematic quartic free energy term and a non-zero stiffness b, only one smectic wavevector is obtained as a function of both depth and temperature, as it shall be shown next.

3.2.4 Saddle-point nematic field profile

Now, we obtain the saddle-point profile with varying temperature, for which one must consider the non-linear quartic term in the nematic action. We had earlier switched to momentum space to facilitate a simple analytical calculation of the strain field correlator. However, armed with the momentum space strain correlator given by Eq.(3.5), we revert back to real space to obtain the defect-generated potential,

$$\begin{aligned} r_{\delta x,z,z'} &= \frac{-g^2\sigma^2}{2(2\pi)} f\left(|z|, |z|', \xi = \frac{\delta x}{|z| + |z|'}, \nu\right) \\ &= \frac{-g^2\sigma^2}{2(2\pi)}\left[\frac{48|z||z|'}{(|z| + |z|')^5}\frac{1 - 10\xi^2 + 5\xi^4}{[\xi^2+1]^5} + \frac{12(2\nu-1)}{(|z| + |z|')^3}\frac{1 - 6\xi^2 + \xi^4}{[\xi^2+1]^4} + \frac{4(2\nu-1)^2}{(|z| + |z|')^3}\frac{1 - 3\xi^2}{[\xi^2+1]^3}\right], \end{aligned} \tag{3.12}$$

where $\delta x = x - x'$. $r_{\delta x,z,z'}$ decays rapidly with increasing mean depth $|z| + |z|'$, but

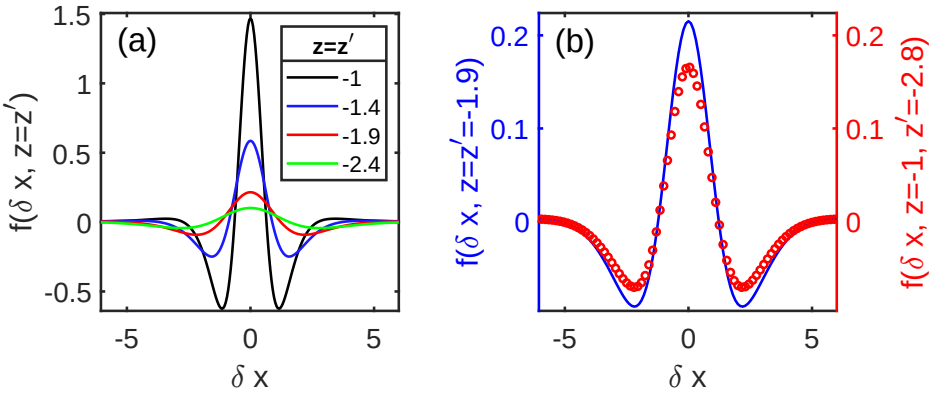

Figure 3.4: The functional form of the defect-generated potential given by Eq.(3.12), barring the constant prefactors outside the braces, with (a) increasing mean depth $(|z|+|z|')/2$, and (b) increasing depth difference $|z|-|z|'$ for the same mean depth. In (a), the width of the central lobe, and the crest to trough distance d_{ct}, scale as the mean depth $\sim |z|+|z|'$. The change in sign over d_{ct} leads to a preference for the nematic field values separated by d_{ct} to assume opposite signs, thereby generatic smecticity.

slowly with the depth difference $|z|-|z|'$, with the decays being algebraic. Importantly, it exhibits an oscillatory behaviour as a function of $\delta x/(z+z')$, with a central peak at $\delta x = 0$ and an algebraically decaying envelope. Consistent with our earlier analysis in momentum space, the important range of $\delta x \sim (|z|+|z|')$, corresponding to $q_x \sim 1/(|z|+|z|')$. Furthermore, as a function of δx, the uniform component vanishes, i.e., $\int_{\delta x} f = 0$. These features are evident from Fig.3.4, showing $r_{\delta x,z,z'}$. The real-space saddle-point equation is now given by,

$$\frac{T-T_\eta^0}{T_\eta^0}\eta_{x,z} - b\partial_z^2\eta_{x,z} - b_\parallel\nabla^2\eta_{x,z} + \int_{x'}\int_{z'\leq 0} r_{x-x',z,z'}\eta_{x',z'} + u_\eta\eta_{x,z}^3 = 0, \qquad (3.13)$$

which is readily solved numerically, following the technique outlined in Sec. 2.2.1, with the results shown in Fig.3.5. As expected, the smectic behaviour nucleates at the surface $z = 0$, eventually decaying into the bulk, giving way to the standard bulk nematic state. Interestingly, the smectic field has the same wavevector q_x as a function of the depth and temperature. This is attributed to the Neumann boundary condition on the nematic field, which prohibits smooth changes in the smectic wavevector, as well as the nematic quartic term, which leads to a bi-quadratic smectic-smectic repulsion for smectic states

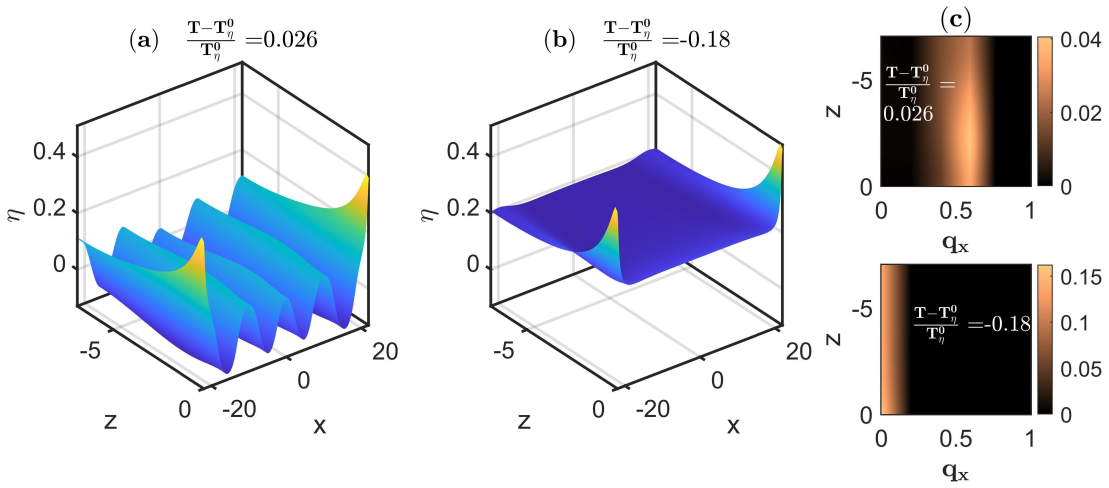

Figure 3.5: The numerical solution to the saddle-point equation Eq.(3.13) in real (a-b) and Fourier space (c), with the reduced temperature $\frac{T-T_\eta^0}{T_\eta^0}$ denoted in the panels. We have considered a sample of dimensions $44 \times 44 \times 7$, along with $b = 0.5$, $b_{\|} = 0.25$, $\frac{(g\sigma)^2}{2} = 1$, and $u_\eta = 5.0$. The lattice has been discretized by considering $N_x = 351$ and $N_z = 56$ cells along the $x-$ and $z-$directions, respectively. Lastly, we have used only the central 72% of the sample while Fourier transforming to discard the boundary artifacts. The Fourier spectrum reveals a smectic component with $q_x^{(s)} \approx 0.57$, with its intensity peaking at $z \approx -2.5$, and decaying subsequently.

with different wavevectors,

$$\int_{\boldsymbol{r}} u_\eta \eta_{\boldsymbol{r}}^4 = 6u_\eta \sum_{q_x, q_x' \neq q_x} |\eta_{q_x}|^2 |\eta_{q_x'}|^2 + \dots . \tag{3.14}$$

As such, the generic case with a finite $b \neq 0$ presents a qualitatively different picture compared to the $b = 0$ case studied previously. Finally, for $T - T_\eta^0 < 0$ the uniform bulk nematic state dominates and erases the smectic signatures. This is, again, caused by the nematic quartic term in the action, this time generating a biquadratic smectic-nematic repulsion ($q_x = q_x^{(s)}$, and $q_x' = 0$ in Eq.(3.14)), thereby penalizing a microscopically coexistent state. Since the smectic free energy gain is a size-independent constant due to the smectic state being localized near the surface, while the nematic free energy gain scales extensively with the system size, only the latter survives in the subcritical saddle-point solution. Lastly, we show the temperature dependence of the nematic and

smectic order parameters in Fig.3.6, which summarizes this discussion. The former is simply defined as the uniform component of the saddle-point solution while the latter is obtained from the peak Fourier component at $q_x^{(s)} \approx 0.57$ on the exposed surface at $z = 0$, as seen in Fig.3.5.

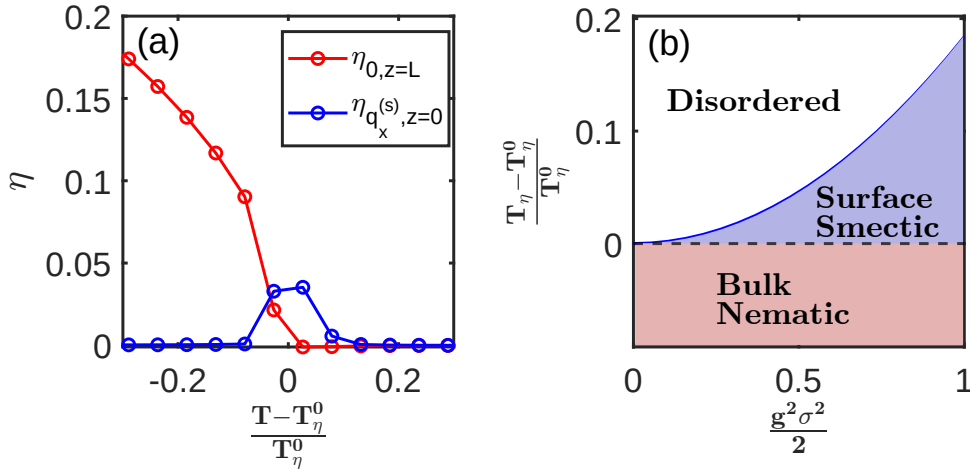

Figure 3.6: (a) The nematic η_0 (red) and the surface smectic $\eta_{q_x^{(s)}}$ (blue) order parameters, extracted from the $q_x = 0$ Fourier component at $z = L = 7$ and the $q_x = q_x^{(s)} \approx 0.57$ Fourier peak height at $z = 0$ in Fig.3.5, respectively. We have only shown the bulk nematic component as the corresponding value at the surface is affected by boundary artefacts. (b) The phase diagram as a function of the effective disorder strength $\frac{(g\sigma)^2}{2}$ and the reduced temperature. The smectic critical temperature scales quadratically with $\frac{(g\sigma)^2}{2}$, as detailed in the supplementary text.

3.3 Conclusion

To conclude, we have proposed a mechanism by which anisotropic elastic defects described by a dipolar force can induce a supercritical incommensurate electronic smectic state, localized near the surface, eventually giving way to the uniform bulk nematic state. The critical smectic wavevector, as well as the associated critical temperature, are found to be dependent only on the elastic parameters of the material. These results, while being significant in light of recent experiments indicating supercritical nematicity as well as smectic behaviour closely related to surface elastic defects, also prompt future studies of novel liquid crystalline instabilities in strongly correlated systems.

Chapter 4

Conclusion and Discussion

To conclude, motivated by the non-linear and non-trivial boundary effects in generic finite-size systems, we have performed a detailed study of the coupled nemato-elastic system in a realistic finite sample glued to a substrate. We have shown that boundary effects lead to significant inhomogeneity in the nematic and strain field profiles, leading to the strains developing primarily near the vertical lateral faces for thin samples. Importantly, we have uncovered a significant suppression of the nematic critical temperature in thin samples due to the stiffness, scaling linearly with the ratio of the sample thickness and width. While providing a new avenue for experimental verification of this interplay between elasticity and nematicity in finite size samples, in the context of the anomalous supercritical nematicity suggested by several experiments, this result is even more surprising as it necessitates alternate mechanisms for supercritical nematicity. In light of this, we propose domains of anisotropic surface elastic defects, such as step defects, as a possible source for supercritical nematicity. Such defects are, in fact, shown to lead to an inhomogeneous supercritical smectic state, with the smectic wavevector determined by the elastic parameters of the material.

Our work, while shedding light on important physics in finite-size systems, also raises several questions for future studies. For instance, on the one hand, it remains to be seen how pure surface phenomena such as Rashba spin-orbit coupling alter the nematic critical temperature while offering distinct experimental signatures. On the other hand, our study motivates new directions for electronic smecticity. A natural continuation would be to consider a theory with coupled smectic bosons and electrons, and subsequently

study the thermodynamic and transport signatures, as well as the effects on fermionic coherence and spectral signatures, which would permit a comparison with ARPES experiments. Additionally, being a finite momentum bosonic order, smecticity is expected to depend indirectly on the Fermi surface topology, as one must now consider the finite momentum properties of the bare nematic action. While the currently employed gradient expansion remains valid for small momenta, it must be modified near the sample surface where our current study predicts a large smectic wavevector.

References

[1] Charles Day. Iron-based superconductors. *Physics Today*, 62(8):36–40, 2009.

[2] Andrey Chubukov and Peter J. Hirschfeld. Iron-based superconductors, seven years later. *Physics Today*, 68(6):46–52, 2015.

[3] Amin Komeili, Abdol Hamid Akbarzadeh, Arezou Doroushi, and Mohammad Reza Eslami. Static analysis of functionally graded piezoelectric beams under thermo-electro-mechanical loads. *Advances in Mechanical Engineering*, 3:153731, 2011.

[4] Rafael M. Fernandes, Peter P. Orth, and Jörg Schmalian. Intertwined Vestigial Order in Quantum Materials: Nematicity and Beyond. *Annual Review of Condensed Matter Physics*, 10(1):133–154, 2019.

[5] R. M. Fernandes, A. V. Chubukov, J. Knolle, I. Eremin, and J. Schmalian. Preemptive nematic order, pseudogap, and orbital order in the iron pnictides. *Phys. Rev. B*, 85:024534, Jan 2012.

[6] T.-M. Chuang, M. P. Allan, Jinho Lee, Yang Xie, Ni Ni, S. L. Bud'ko, G. S. Boebinger, P. C. Canfield, and J. C. Davis. Nematic Electronic Structure in the "Parent" State of the Iron-Based Superconductor $Ca(Fe_{1-x}Co_x)_2As_2$. *Science*, 327(5962):181–184, 2010.

[7] Anna E. Böhmer and Christoph Meingast. Electronic nematic susceptibility of iron-based superconductors. *Comptes Rendus Physique*, 17(1):90–112, 2016.

[8] Jiun-Haw Chu, Hsueh-Hui Kuo, James G. Analytis, and Ian R. Fisher. Divergent Nematic Susceptibility in an Iron Arsenide Superconductor. *Science*, 337(6095):710–712, 2012.

[9] H. Murayama, Y. Sato, R. Kurihara, S. Kasahara, Y. Mizukami, Y. Kasahara, H. Uchiyama, A. Yamamoto, E.-G. Moon, J. Cai, J. Freyermuth, M. Greven, T. Shibauchi, and Y. Matsuda. Diagonal nematicity in the pseudogap phase of $HgBa_2CuO_{4+\delta}$. *Nature Communications*, 10(1):3282, Jul 2019.

[10] Laimei Nie, Gilles Tarjus, and Steven Allan Kivelson. Quenched disorder and vestigial nematicity in the pseudogap regime of the cuprates. *Proceedings of the National Academy of Sciences of the United States of America*, 111(22):79807985, June 2014.

[11] R. Daou, J. Chang, David LeBoeuf, Olivier Cyr-Choinière, Francis Laliberté, Nicolas Doiron-Leyraud, B. J. Ramshaw, Ruixing Liang, D. A. Bonn, W. N. Hardy, and Louis Taillefer. Broken rotational symmetry in the pseudogap phase of a high-Tc superconductor. *Nature*, 463(7280):519–522, Jan 2010.

[12] M. J. Lawler, K. Fujita, Jhinhwan Lee, A. R. Schmidt, Y. Kohsaka, Chung Koo Kim, H. Eisaki, S. Uchida, J. C. Davis, J. P. Sethna, and Eun-Ah Kim. Intra-unit-cell electronic nematicity of the high-Tc copper-oxide pseudogap states. *Nature*, 466(7304):347–351, Jul 2010.

[13] Matthias Vojta. Lattice symmetry breaking in cuprate superconductors: stripes, nematics, and superconductivity. *Advances in Physics*, 58(6):699–820, 2009.

[14] Fujita, Kazuhiro and Hamidian, Mohammad H. and Edkins, Stephen D. and Kim, Chung Koo and Kohsaka, Yuhki and Azuma, Masaki and Takano, Mikio and Takagi, Hidenori and Eisaki, Hiroshi and Uchida, Shin-ichi and Allais, Andrea and Lawler, Michael J. and Kim, Eun-Ah and Sachdev, Subir and Davis, J. C. Séamus. Direct phase-sensitive identification of a d-form factor density wave in underdoped cuprates. *Proceedings of the National Academy of Sciences*, 111(30):E3026–E3032, 2014.

[15] Kohsaka, Y. and Taylor, C. and Fujita, K. and Schmidt, A. and Lupien, C. and Hanaguri, T. and Azuma, M. and Takano, M. and Eisaki, H. and Takagi, H. and Uchida, S. and Davis, J. C. An Intrinsic Bond-Centered Electronic Glass with Unidirectional Domains in Underdoped Cuprates. *Science*, 315(5817):1380–1385, 2007.

[16] Jun Zhao, D. T. Adroja, Dao-Xin Yao, R. Bewley, Shiliang Li, X. F. Wang, G. Wu, X. H. Chen, Jiangping Hu, and Pengcheng Dai. Spin waves and magnetic exchange interactions in $CaFe_2As_2$. *Nature Physics*, 5(8):555–560, Aug 2009.

[17] C. Lester, Jiun-Haw Chu, J. G. Analytis, S. C. Capelli, A. S. Erickson, C. L. Condron, M. F. Toney, I. R. Fisher, and S. M. Hayden. Neutron scattering study of the interplay between structure and magnetism in $Ba(Fe_{1-x}Co_x)_2As_2$. *Phys. Rev. B*, 79:144523, Apr 2009.

[18] A. Kreyssig, M. G. Kim, S. Nandi, D. K. Pratt, W. Tian, J. L. Zarestky, N. Ni, A. Thaler, S. L. Bud'ko, P. C. Canfield, R. J. McQueeney, and A. I. Goldman. Suppression of antiferromagnetic order and orthorhombic distortion in superconducting $Ba(Fe_{0.961}Rh_{0.039})_2As_2$. *Phys. Rev. B*, 81:134512, Apr 2010.

[19] C. Lester, Jiun-Haw Chu, J. G. Analytis, S. C. Capelli, A. S. Erickson, C. L. Condron, M. F. Toney, I. R. Fisher, and S. M. Hayden. Erratum: Neutron scattering study of the interplay between structure and magnetism in $Ba(Fe_{1-x}Co_x)_2As_2$ [Phys. Rev. B 79, 144523 (2009)]. *Phys. Rev. B*, 80:229901, Dec 2009.

[20] Jiun-Haw Chu, James G. Analytis, Kristiaan De Greve, Peter L. McMahon, Zahirul Islam, Yoshihisa Yamamoto, and Ian R. Fisher. In-Plane Resistivity Anisotropy in an Underdoped Iron Arsenide Superconductor. *Science*, 329(5993):824–826, 2010.

[21] M. A. Tanatar, E. C. Blomberg, A. Kreyssig, M. G. Kim, N. Ni, A. Thaler, S. L. Bud'ko, P. C. Canfield, A. I. Goldman, I. I. Mazin, and R. Prozorov. Uniaxial-strain mechanical detwinning of $CaFe_2As_2$ and $BaFe_2As_2$ crystals: Optical and transport study. *Phys. Rev. B*, 81:184508, May 2010.

[22] Ming Yi, Donghui Lu, Jiun-Haw Chu, James G. Analytis, Adam P. Sorini, Alexander F. Kemper, Brian Moritz, Sung-Kwan Mo, Rob G. Moore, Makoto Hashimoto, Wei-Sheng Lee, Zahid Hussain, Thomas P. Devereaux, Ian R. Fisher, and Zhi-Xun Shen. Symmetry-breaking orbital anisotropy observed for detwinned $Ba(Fe_{1-x}Co_x)_2As_2$ above the spin density wave transition. *Proceedings of the National Academy of Sciences*, 108(17):6878–6883, 2011.

[23] Xiao Chen, S. Maiti, R. M. Fernandes, and P. J. Hirschfeld. Nematicity and superconductivity: Competition versus cooperation. *Phys. Rev. B*, 102:184512, Nov 2020.

[24] Rafael M. Fernandes and Andrew J. Millis. Nematicity as a Probe of Superconducting Pairing in Iron-Based Superconductors. *Phys. Rev. Lett.*, 111:127001, Sep 2013.

[25] S. Teknowijoyo, K. Cho, M. A. Tanatar, J. Gonzales, A. E. Böhmer, O. Cavani, V. Mishra, P. J. Hirschfeld, S. L. Bud'ko, P. C. Canfield, and R. Prozorov. Enhancement of superconducting transition temperature by pointlike disorder and anisotropic energy gap in FeSe single crystals. *Phys. Rev. B*, 94:064521, Aug 2016.

[26] S. Nandi, M. G. Kim, A. Kreyssig, R. M. Fernandes, D. K. Pratt, A. Thaler, N. Ni, S. L. Bud'ko, P. C. Canfield, J. Schmalian, R. J. McQueeney, and A. I. Goldman. Anomalous Suppression of the Orthorhombic Lattice Distortion in Superconducting $Ba(Fe_{1-x}Co_x)_2As_2$ Single Crystals. *Phys. Rev. Lett.*, 104:057006, Feb 2010.

[27] A. E. Böhmer, F. Hardy, F. Eilers, D. Ernst, P. Adelmann, P. Schweiss, T. Wolf, and C. Meingast. Lack of coupling between superconductivity and orthorhombic distortion in stoichiometric single-crystalline FeSe. *Phys. Rev. B*, 87:180505, May 2013.

[28] Liran Wang, Frdric Hardy, Thomas Wolf, Peter Adelmann, Rainer Fromknecht, Peter Schweiss, and Christoph Meingast. Superconductivity-enhanced nematicity and s+d gap symmetry in $Fe(Se_{1-x}S_x)$. *physica status solidi (b)*, 254(1):1600153, 2017.

[29] P. O. Sprau, A. Kostin, A. Kreisel, A. E. Böhmer, V. Taufour, P. C. Canfield, S. Mukherjee, P. J. Hirschfeld, B. M. Andersen, and J. C. Séamus Davis. Discovery of orbital-selective Cooper pairing in FeSe. *Science*, 357(6346):75–80, 2017.

[30] R. M. Fernandes, L. H. VanBebber, S. Bhattacharya, P. Chandra, V. Keppens, D. Mandrus, M. A. McGuire, B. C. Sales, A. S. Sefat, and J. Schmalian. Effects of Nematic Fluctuations on the Elastic Properties of Iron Arsenide Superconductors. *Phys. Rev. Lett.*, 105:157003, Oct 2010.

[31] Rafael M. Fernandes, Anna E. Böhmer, Christoph Meingast, and Jörg Schmalian. Scaling between Magnetic and Lattice Fluctuations in Iron Pnictide Superconductors. *Phys. Rev. Lett.*, 111:137001, Sep 2013.

[32] Aaron Patz, Tianqi Li, Sheng Ran, Rafael M. Fernandes, Jörg Schmalian, Sergey L. Bud'ko, Paul C. Canfield, Ilias E. Perakis, and Jigang Wang. Ultrafast observation of critical nematic fluctuations and giant magnetoelastic coupling in iron pnictides. *Nature Communications*, 5(1):3229, Feb 2014.

[33] A. M. Merritt, F. Weber, J.-P. Castellan, Th. Wolf, D. Ishikawa, A. H. Said, A. Alatas, R. M. Fernandes, A. Q. R. Baron, and D. Reznik. Nematic Correlation Length in Iron-Based Superconductors Probed by Inelastic X-Ray Scattering. *Phys. Rev. Lett.*, 124:157001, Apr 2020.

[34] Masahito Yoshizawa, Daichi Kimura, Taiji Chiba, Shalamujiang Simayi, Yoshiki Nakanishi, Kunihiro Kihou, Chul-Ho Lee, Akira Iyo, Hiroshi Eisaki, Masamichi Nakajima, and Shin-ichi Uchida. Structural Quantum Criticality and Superconductivity in Iron-Based Superconductor $Ba(Fe_{1-x}Co_x)_2As_2$. *Journal of the Physical Society of Japan*, 81(2):024604, 2012.

[35] Terutaka Goto, Ryosuke Kurihara, Koji Araki, Keisuke Mitsumoto, Mitsuhiro Akatsu, Yuichi Nemoto, Shunichi Tatematsu, and Masatoshi Sato. Quadrupole Effects of Layered Iron Pnictide Superconductor $Ba(Fe_{0.9}Co_{0.1})_2As_2$. *Journal of the Physical Society of Japan*, 80(7):073702, 2011.

[36] S. Chibani, D. Farina, P. Massat, M. Cazayous, A. Sacuto, T. Urata, Y. Tanabe, K. Tanigaki, A. E. Böhmer, P. C. Canfield, M. Merz, S. Karlsson, P. Strobel, P. Toulemonde, I. Paul, and Y. Gallais. Lattice-shifted nematic quantum critical point in $FeSe_{1-x}S_x$. *npj Quantum Materials*, 6(1):37, Apr 2021.

[37] Chetan Dhital, Tom Hogan, Z. Yamani, Robert J. Birgeneau, W. Tian, M. Matsuda, A. S. Sefat, Ziqiang Wang, and Stephen D. Wilson. Evolution of antiferromagnetic susceptibility under uniaxial pressure in $Ba(Fe_{1-x}Co_x)_2As_2$. *Phys. Rev. B*, 89:214404, Jun 2014.

[38] S. Kasahara, H. J. Shi, K. Hashimoto, S. Tonegawa, Y. Mizukami, T. Shibauchi, K. Sugimoto, T. Fukuda, T. Terashima, Andriy H. Nevidomskyy, and Y. Matsuda. Electronic nematicity above the structural and superconducting transition in $BaFe_2(As_{1-x}P_x)_2$. *Nature*, 486(7403):382–385, Jun 2012.

[39] Eric Thewalt, Ian M. Hayes, James P. Hinton, Arielle Little, Shreyas Patankar, Liang Wu, Toni Helm, Camelia V. Stan, Nobumichi Tamura, James G. Analytis, and Joseph Orenstein. Imaging Anomalous Nematic Order and Strain in Optimally Doped $BaFe_2(As, P)_2$. *Phys. Rev. Lett.*, 121:027001, Jul 2018.

[40] Tetsuya Iye, Marc-Henri Julien, Hadrien Mayaffre, Mladen Horvati, Claude Berthier, Kenji Ishida, Hiroaki Ikeda, Shigeru Kasahara, Takasada Shibauchi, and Yuji Matsuda. Emergence of Orbital Nematicity in the Tetragonal Phase of $BaFe_2(As_{1-x}P_x)_2$. *Journal of the Physical Society of Japan*, 84(4):043705, 2015.

[41] E. P. Rosenthal, E. F. Andrade, C. J. Arguello, R. M. Fernandes, L. Y. Xing, X. C. Wang, C. Q. Jin, A. J. Millis, and A. N. Pasupathy. Visualization of electron nematicity and unidirectional antiferroic fluctuations at high temperatures in NaFeAs. *Nature Physics*, 10(3):225–232, Mar 2014.

[42] Haoran Man, Xingye Lu, Justin S. Chen, Rui Zhang, Wenliang Zhang, Huiqian Luo, J. Kulda, A. Ivanov, T. Keller, Emilia Morosan, Qimiao Si, and Pengcheng Dai. Electronic nematic correlations in the stress-free tetragonal state of $BaFe_{2-x}Ni_xAs_2$. *Phys. Rev. B*, 92:134521, Oct 2015.

[43] L. Stojchevska, T. Mertelj, Jiun-Haw Chu, Ian R. Fisher, and D. Mihailovic. Doping dependence of femtosecond quasiparticle relaxation dynamics in $Ba(Fe,Co)_2As_2$ single crystals: Evidence for normal-state nematic fluctuations. *Phys. Rev. B*, 86:024519, Jul 2012.

[44] T. Shimojima, T. Sonobe, W. Malaeb, K. Shinada, A. Chainani, S. Shin, T. Yoshida, S. Ideta, A. Fujimori, H. Kumigashira, K. Ono, Y. Nakashima, H. Anzai, M. Arita, A. Ino, H. Namatame, M. Taniguchi, M. Nakajima, S. Uchida,

Y. Tomioka, T. Ito, K. Kihou, C. H. Lee, A. Iyo, H. Eisaki, K. Ohgushi, S. Kasahara, T. Terashima, H. Ikeda, T. Shibauchi, Y. Matsuda, and K. Ishizaka. Pseudogap formation above the superconducting dome in iron pnictides. *Phys. Rev. B*, 89:045101, Jan 2014.

[45] T. Sonobe, T. Shimojima, A. Nakamura, M. Nakajima, S. Uchida, K. Kihou, C. H. Lee, A. Iyo, H. Eisaki, K. Ohgushi, and K. Ishizaka. Orbital-anisotropic electronic structure in the nonmagnetic state of $BaFe_2(As_{1-x}P_x)_2$ superconductors. *Scientific Reports*, 8(1):2169, Feb 2018.

[46] P. Zhang, T. Qian, P. Richard, X. P. Wang, H. Miao, B. Q. Lv, B. B. Fu, T. Wolf, C. Meingast, X. X. Wu, Z. Q. Wang, J. P. Hu, and H. Ding. Observation of two distinct d_{xz}/d_{yz} band splittings in FeSe. *Phys. Rev. B*, 91:214503, Jun 2015.

[47] Masayuki Toyoda, Yoshiaki Kobayashi, and Masayuki Itoh. Nematic fluctuations in iron arsenides NaFeAs and LiFeAs probed by ^{75}As NMR. *Phys. Rev. B*, 97:094515, Mar 2018.

[48] P. Wiecki, M. Nandi, A. E. Böhmer, S. L. Bud'ko, P. C. Canfield, and Y. Furukawa. NMR evidence for static local nematicity and its cooperative interplay with low-energy magnetic fluctuations in FeSe under pressure. *Phys. Rev. B*, 96:180502, Nov 2017.

[49] P. S. Wang, P. Zhou, S. S. Sun, Y. Cui, T. R. Li, Hechang Lei, Ziqiang Wang, and Weiqiang Yu. Robust short-range-ordered nematicity in FeSe evidenced by high-pressure NMR. *Phys. Rev. B*, 96:094528, Sep 2017.

[50] Maria N. Gastiasoro, I. Paul, Y. Wang, P. J. Hirschfeld, and Brian M. Andersen. Emergent Defect States as a Source of Resistivity Anisotropy in the Nematic Phase of Iron Pnictides. *Phys. Rev. Lett.*, 113:127001, Sep 2014.

[51] Y. Wang, Maria N. Gastiasoro, Brian M. Andersen, M. Tomić, Harald O. Jeschke, Roser Valentí, Indranil Paul, and P. J. Hirschfeld. Effects of Lifshitz Transition on Charge Transport in Magnetic Phases of Fe-Based Superconductors. *Phys. Rev. Lett.*, 114:097003, Mar 2015.

[52] S.-H. Baek, D. V. Efremov, J. M. Ok, J. S. Kim, Jeroen van den Brink, and B. Büchner. Nematicity and in-plane anisotropy of superconductivity in $\beta - \mathrm{FeSe}$ detected by ^{77}Se nuclear magnetic resonance. *Phys. Rev. B*, 93:180502, May 2016.

[53] Chih-Wei Luo, Po Chung Cheng, Shun-Hung Wang, Jen-Che Chiang, Jiunn-Yuan Lin, Kaung-Hsiung Wu, Jenh-Yih Juang, Dmitry A. Chareev, Olga S. Volkova, and Alexander N. Vasiliev. Unveiling the hidden nematicity and spin subsystem in FeSe. *npj Quantum Materials*, 2(1):32, Jun 2017.

[54] X. Luo, V. Stanev, B. Shen, L. Fang, X. S. Ling, R. Osborn, S. Rosenkranz, T. M. Benseman, R. Divan, W.-K. Kwok, and U. Welp. Antiferromagnetic and nematic phase transitions in $BaFe_2(As_{1-x}P_x)_2$ studied by ac microcalorimetry and SQUID magnetometry. *Phys. Rev. B*, 91:094512, Mar 2015.

[55] Jiun-Haw Chu, James G. Analytis, Chris Kucharczyk, and Ian R. Fisher. Determination of the phase diagram of the electron-doped superconductor $Ba(Fe_{1-x}Co_x)_2As_2$. *Phys. Rev. B*, 79:014506, Jan 2009.

[56] Kok Wee Song and Alexei E. Koshelev. Surface nematic order in iron pnictides. *Phys. Rev. B*, 94:094509, Sep 2016.

[57] P. M. Chaikin and T. C. Lubensky. *Principles of Condensed Matter Physics*. Cambridge University Press, 1995.

[58] Daniel Steffensen, Panagiotis Kotetes, Indranil Paul, and Brian M. Andersen. Disorder-induced electronic nematicity. *Phys. Rev. B*, 100:064521, Aug 2019.

[59] A. Kostin, P. O. Sprau, A. Kreisel, Yi Xue Chong, A. E. Böhmer, P. C. Canfield, P. J. Hirschfeld, B. M. Andersen, and J. C. Séamus Davis. Imaging orbital-selective quasiparticles in the Hund's metal state of FeSe. *Nature Materials*, 17(10):869–874, Oct 2018.

[60] M. P. Allan, T.-M. Chuang, F. Massee, Yang Xie, Ni Ni, S. L. Bud'ko, G. S. Boebinger, Q. Wang, D. S. Dessau, P. C. Canfield, M. S. Golden, and J. C. Davis. Anisotropic impurity states, quasiparticle scattering and nematic transport in underdoped $Ca(Fe_{1-x}Co_x)_2As_2$. *Nature Physics*, 9(4):220–224, Apr 2013.

[61] S. Grothe, Shun Chi, P. Dosanjh, Ruixing Liang, W. N. Hardy, S. A. Burke, D. A. Bonn, and Y. Pennec. Bound states of defects in superconducting LiFeAs studied by scanning tunneling spectroscopy. *Phys. Rev. B*, 86:174503, Nov 2012.

[62] Xiaodong Zhou, Cun Ye, Peng Cai, Xiangfeng Wang, Xianhui Chen, and Yayu Wang. Quasiparticle Interference of C_2-Symmetric Surface States in a LaOFeAs Parent Compound. *Phys. Rev. Lett.*, 106:087001, Feb 2011.

[63] M. I. Kaganov and N. S. Karpinskaya. Role of surface energy in the phase transition from the paramagnetic state to the ferromagnetic . *JETP Lett.*, 49:1083, 1979. [ZhETF, Vol. 76, No. 6, p. 2143, June 1979].

[64] T. C. Lubensky and Morton H. Rubin. Critical phenomena in semi-infinite systems. I. ϵ expansion for positive extrapolation length. *Phys. Rev. B*, 11:4533–4546, Jun 1975.

[65] T. C. Lubensky and Morton H. Rubin. Critical phenomena in semi-infinite systems. II. Mean-field theory. *Phys. Rev. B*, 12:3885–3901, Nov 1975.

[66] K. Binder and P. C. Hohenberg. Phase Transitions and Static Spin Correlations in Ising Models with Free Surfaces. *Phys. Rev. B*, 6:3461–3487, Nov 1972.

[67] D. L. Mills. Surface Effects in Magnetic Crystals near the Ordering Temperature. *Phys. Rev. B*, 3:3887–3895, Jun 1971.

[68] Michael E. Fisher and Michael N. Barber. Scaling Theory for Finite-Size Effects in the Critical Region. *Phys. Rev. Lett.*, 28:1516–1519, Jun 1972.

[69] R. M. Fernandes, A. V. Chubukov, and J. Schmalian. What drives nematic order in iron-based superconductors? *Nature Physics*, 10(2):97–104, Feb 2014.

[70] Rafael M Fernandes and Jörg Schmalian. Manifestations of nematic degrees of freedom in the magnetic, elastic, and superconducting properties of the iron pnictides. *Superconductor Science and Technology*, 25(8):084005, jul 2012.

[71] R. Zhou, L. Y. Xing, X. C. Wang, C. Q. Jin, and Guo-qing Zheng. Orbital order and spin nematicity in the tetragonal phase of the electron-doped iron pnictides $NaFe_{1-x}Co_xAs$. *Phys. Rev. B*, 93:060502, Feb 2016.

[72] Xiao Ren, Lian Duan, Yuwen Hu, Jiarui Li, Rui Zhang, Huiqian Luo, Pengcheng Dai, and Yuan Li. Nematic Crossover in $BaFe_2As_2$ under Uniaxial Stress. *Phys. Rev. Lett.*, 115:197002, Nov 2015.

[73] Tobias Holder and Walter Metzner. Incommensurate nematic fluctuations in two-dimensional metals. *Phys. Rev. B*, 85:165130, Apr 2012.

[74] Christoph Husemann and Walter Metzner. Incommensurate nematic fluctuations in the two-dimensional Hubbard model. *Phys. Rev. B*, 86:085113, Aug 2012.

[75] S. Bulut, W. A. Atkinson, and A. P. Kampf. Spatially modulated electronic nematicity in the three-band model of cuprate superconductors. *Phys. Rev. B*, 88:155132, Oct 2013.

[76] Subir Sachdev and Rolando La Placa. Bond Order in Two-Dimensional Metals with Antiferromagnetic Exchange Interactions. *Phys. Rev. Lett.*, 111:027202, Jul 2013.

[77] Max A. Metlitski and Subir Sachdev. Quantum phase transitions of metals in two spatial dimensions. II. Spin density wave order. *Phys. Rev. B*, 82:075128, Aug 2010.

[78] Max A Metlitski and Subir Sachdev. Instabilities near the onset of spin density wave order in metals. *New Journal of Physics*, 12(10):105007, oct 2010.

[79] Andrea Allais, Johannes Bauer, and Subir Sachdev. Density wave instabilities in a correlated two-dimensional metal. *Phys. Rev. B*, 90:155114, Oct 2014.

[80] Hae-Young Kee, Christoph M Puetter, and David Stroud. Transport signatures of electronic-nematic stripe phases. *Journal of Physics: Condensed Matter*, 25(20):202201, apr 2013.

[81] Yonghao Yuan, Xuemin Fan, Xintong Wang, Ke He, Yan Zhang, Qi-Kun Xue, and Wei Li. Incommensurate smectic phase in close proximity to the high-Tc superconductor FeSe/SrTiO3. *Nature Communications*, 12(1):2196, Apr 2021.

[82] Wei Li, Yan Zhang, Peng Deng, Zhilin Xu, S.-K. Mo, Ming Yi, Hao Ding, M. Hashimoto, R. G. Moore, D.-H. Lu, Xi Chen, Z.-X. Shen, and Qi-Kun Xue.

Stripes developed at the strong limit of nematicity in FeSe film. *Nature Physics*, 13(10):957–961, Oct 2017.

[83] Chi Ming Yim, Christopher Trainer, Ramakrishna Aluru, Shun Chi, Walter N. Hardy, Ruixing Liang, Doug Bonn, and Peter Wahl. Discovery of a strain-stabilised smectic electronic order in LiFeAs. *Nature Communications*, 9(1):2602, Jul 2018.

[84] V.I. Marchenko and A. Ya. Parshin. Elastic properties of crystal surfaces. *JETP Lett.*, 52:129, 1980. [ZhETF, Vol. 79, No. 1, p. 257, July 1980].

[85] L. E. Shilkrot and D. J. Srolovitz. Elastic field of a surface step: Atomistic simulations and anisotropic elastic theory. *Phys. Rev. B*, 53:11120–11127, Apr 1996.

[86] John Stewart, Oliver Pohland, and J. Murray Gibson. Elastic-displacement field of an isolated surface step. *Phys. Rev. B*, 49:13848–13858, May 1994.

[87] Arnold M Kosevich. *The Crystal Lattice: Phonons, Solitons, Dislocations, Superlattices*. WILEY-VCH Verlag GmbH & Co. KGaA, 2005.

[88] D.J. Bacon, D.M. Barnett, and R.O. Scattergood. Anisotropic continuum theory of lattice defects. *Progress in Materials Science*, 23:51–262, 1980.

[89] Emmanuel Clouet, Cline Varvenne, and Thomas Jourdan. Elastic modeling of point-defects and their interaction. *Computational Materials Science*, 147:49–63, 2018.

[90] Cristian Teodosiu. *Elastic Models of Crystal Defects*. Springer Berlin Heidelberg, 1982.

[91] E.M. Lifshitz, A.M. Kosevich, and L.P. Pitaevskii. *Theory of Elasticity*. Butterworth-Heinemann, 1986.

[92] R. A. Cowley. Acoustic phonon instabilities and structural phase transitions. *Phys. Rev. B*, 13:4877–4885, June 1976.

[93] Christopher Max. *Master thesis*. Universität zu Köln, 2015.

[94] S. Timoshenko and S. Woinowsky-Krieger. *Theory of Plates and Shells*. McGraw-Hill, 2nd edition, 1959.

[95] S. G. Lekhnitskii, T. Cheron, and S. Tsai. *Anisotropic Plates*. Gordon and Breach Science Publishers, 1st edition, 1968.

Appendix A

Variational minimization in finite domains: Boundary conditions

A.1 Continuum Set-up

The standard problem statement in variational minimization consists of an energy/action ($S = \int_M \mathcal{S}[\phi]$) functional defined in terms of a field ϕ over a domain M along with certain boundary conditions on ∂M. Refraining from an overly general discussion, we restrict ourselves to quadratic action functionals of the kind encountered in our study $\mathcal{S} = \int_M \left(\frac{1}{2}(\nabla\phi)^2 + \frac{1}{2}a\phi^2\right) + \frac{1}{2}a^s\phi^2|_{\partial M}$, to focus on the implementation of various boundary conditions.

We take a moment to remark on the last term, which is a surface term, with a^s being the surface mass/energy. Such contributions generally arise when the bulk mass a changes discontinuously at the surface. Being a measure zero set, the discontinuously altered value of a only at the surface is not captured by the spatial integral. As such, we designate $a^s = a_{\boldsymbol{r}=\partial M} - \lim_{\boldsymbol{r}\to\partial_M} a$, which is the difference of the actual surface value of a, and the extrapolated limit of the bulk a.

For simplicity, we consider a one dimensional domain given by the interval $[0, L]$, with the action,

$$S = \int_0^L dz\Big(\frac{1}{2}C(\nabla\phi)^2 + \frac{1}{2}a\phi^2\Big) + \frac{1}{2}a^s\phi_0^2 + \frac{1}{2}a^s\phi_L^2, \tag{A.1}$$

where the last two terms are surface terms, which shall be used for the case of Robin boundary conditions. In the following subsections, we consider field governed by this action and describe the implementation of various boundary conditions relevant to us.

A.2 Boundary conditions

There are primarily two kinds of boundary conditions: essential and natural, which are aptly named based on their technique of implementation. Additionally, we also consider Robin boundary conditions, which is a combination of the two. In this section we go over each one of them one by one. Setting the variation of the action to zero, $\delta S = S[\phi + \delta\phi] - S[\phi] = 0$, yields,

$$\int_0^L dz \Big([C\partial_z \phi]\partial_z \delta\phi + a\phi\delta\phi \Big) = \int_0^L dz \Big([-C\partial_z^2 + a\phi]\delta\phi \Big) + (C\partial_z\phi)\delta\phi|_0^L = 0. \tag{A.2}$$

The requirement that the variation vanishes imposes two conditions. First, irrespective of the boundary conditions, the bulk contribution must vanish, $-C\partial_z^2 + a\phi$. Second, the surface contribution, which is the product of the boundary derivative and the boundary variation of the field, mush vanish. This may either happen if the boundary value is fixed (or periodic) or if the boundary derivative vanishes, which correspond to the Dirichlet and Neumann condition, respectively. As described in the following subsections, this surface term, in conjunction with suitably added surface contributions, are able to introduce the required boundary conditions depending on which part is forced to vanish.

A.2.1 Essential boundary condition

Essential boundary conditions, or more commonly Dirichlet boundary conditions, constitute the specification of the field values on the boundaries. These conditions are essential in the sense that they must either be incorporated from the outset by choosing the basis functions appropriately, or enforced explicitly using Lagrange multipliers.

In Eq. (A.2), fixing the boundary value of ϕ is sufficient for the surface term to vanish, which can then be safely dropped. However, directly dropping the surface term while keeping the boundary values unconstrained implicitly implies that the boundary derivatives vanish, instead. Hence, Dirichlet conditions must be explicitly imposed.

This may either be done by directly employing a basis set of functions satisfying the condition to form the variations, or by the use of Lagrange multipliers.

A.2.2 Natural boundary conditions

Natural boundary conditions, or more commonly Neumann boundary conditions, enforce that the field derivatives vanish on the boundaries. Additionally, there are generalized Neumann boundary conditions, in which the field derivatives on the boundaries are required to assume a specific constant value.

For the standard Neumann boundary conditions involving vanishing boundary derivatives, we simply retain only the bulk contribution in Eq. (A.2). As already described in the previous subsection, dropping the surface term while letting the boundary value be unconstrained is tantamount to enforcing Neumann conditions. However, for the generalized Neumann condition $\partial_z\phi_L = b_L$ and $\partial_z\phi_0 = b_0$, a surface term must be added. Since the field derivative is automatically generated from the gradient term, it only remains for the action to be modified by adding the surface term $Cb_0\phi_0 - Cb_L\phi_L$. Hence, from Eq. (A.2),

$$\delta S = \int_0^L dz\Big([-C\partial_z^2 + a\phi]\delta\phi\Big) + (C\partial_z\phi)\delta\phi|_0^L + Cb_0\delta\phi_0 - Cb_L\delta\phi_L) = 0, \tag{A.3}$$

$$\therefore \partial_z\phi_L = b_L, \quad \partial_z\phi_0 = b_0. \tag{A.4}$$

These are natural in the sense that neglecting surface terms in the variation of the suitably constructed action naturally/automatically leads to vanishing derivatives on the boundaries.

A.2.3 Robin boundary conditions

Finally, Robin boundary conditions specify the boundary derivatives in terms of the boundary values of the field. Like the generalized Neumann conditions described earlier, Robin conditions are imposed by the addition of suitable surface terms. Once again, since the field derivative is automatically generated from the gradient term, the action

is modified by adding the surface term $\frac{1}{2}Cb_0\phi_0^2 - \frac{1}{2}Cb_L\phi_L^2$. Hence, from Eq. (A.2),

$$\delta S = \int_0^L dz\Big([-C\partial_z^2 + a\phi]\delta\phi\Big) + (C\partial_z\phi)\delta\phi|_0^L + Cb_0\phi_0\delta\phi_0 - Cb_L\phi_L\delta\phi_L) = 0, \quad \text{(A.5)}$$

$$\therefore C\partial\phi_L = b_L\phi_L, \quad C\partial\phi_0 = b_0\phi_0. \quad \text{(A.6)}$$

A.3 Discrete set-up

Alongside the continuum set-up illustrated above, the discrete formulation is more useful to highlight the numerical implementation. Additionally, it is easier to see the boundary terms, which for a three-dimensional set-up, contains faces, edges, and vertices. Beginning with the same action,

$$S = \sum_j \Delta_x \frac{1}{2} C\left(\frac{(\phi_j - \phi_{j-1})}{\Delta_x}\right)^2 + \frac{1}{2}a\phi_j^2 + \frac{1}{2}a^s\phi_1^2 + \frac{1}{2}a^s\phi_N^2, \quad \text{(A.7)}$$

the variational derivative with respect to ϕ_j yields the bulk equation,

$$\frac{\delta S}{\delta\phi_j} = C\frac{2\phi_j - \phi_j - \phi_{j+1}}{\Delta_x^2} + a\phi_j = 0, \quad \implies -C\partial_x^2\phi + a\phi = 0 \quad \text{(A.8)}$$

while for the boundaries, due to the lack of a bond/gradient-term along on one side of the chosen index j,

$$\frac{\delta S}{\delta\phi_j} = \begin{cases} C\frac{\phi_N - \phi_{N-1}}{\Delta_x} + a^s\phi_N = 0, & \implies \phi_N = \frac{\phi_{N-1}}{1+\frac{a^s}{C}\Delta_x}, \quad \equiv C\partial_x\phi|_{x=L} + a^s\phi_{x=L} = 0, \\ C\frac{\phi_1 - \phi_2}{\Delta_x} + a^s\phi_1 = 0, & \implies \phi_1 = \frac{\phi_2}{1+\frac{a^s}{C}\Delta_x}, \quad \equiv -C\partial_x\phi|_{x=0} + a^s\phi_{x=0} = 0 \end{cases}. \quad \text{(A.9)}$$

Clearly, a negative surface energy $a^s < 0$ enhances the surface field values. This effect is propagated to the bulk, as the bulk saddle-point equation refers to the boundary values through the bulk Laplacian.

It is readily extended to higher dimensions. For instance, for a three-dimensional

cubical system of size $(L_x \times L_y \times L_z)$ with (N_x, N_y, N_z) lattice sites,

$$\begin{aligned} S = &\sum_j \Delta_x\Delta_y\Delta_z \Bigg[C_x \frac{1}{2}\left(\frac{(\phi_{[j_x,j_y,j_z]} - \phi_{[j_x-1,j_y,j_z]})}{\Delta_x}\right)^2 + C_y \frac{1}{2}\left(\frac{(\phi_{[j_x,j_y,j_z]} - \phi_{[j_x,j_y-1,j_z]})}{\Delta_y}\right)^2 \\ &+ C_z \frac{1}{2}\left(\frac{(\phi_{[j_x,j_y,j_z]} - \phi_{[j_x,j_y,j_z-1]})}{\Delta_z}\right)^2\Bigg] + \frac{1}{2}a\phi^2_{[j_x,j_y,j_z]} + \frac{1}{2}a^s_x\phi^2_{[1,j_y,j_z]} + \frac{1}{2}a^s_y\phi^2_{[j_x,1,j_z]} \\ &+ \frac{1}{2}a^s_z\phi^2_{[j_x,j_y,1]} + \frac{1}{2}a^s_x\phi^2_{[N_x,j_y,j_z]} + \frac{1}{2}a^s_y\phi^2_{[j_x,N_y,j_z]} + \frac{1}{2}a^s_z\phi^2_{[j_x,j_y,N_z]}. \end{aligned} \tag{A.10}$$

To obtain the bulk saddle-point equation, note that each site j is connected to two neighbors along each direction, with the corresponding terms in the action being, $\sum_{\mu=x,y,z}\left(\frac{\phi_{[j_x,j_y,j_z]}-\phi_{[j_x,j_y,j_z]-1_\mu}}{\Delta_\mu}\right)^2 + \left(\frac{\phi_{[j_x,j_y,j_z]}-\phi_{[j_x,j_y,j_z]+1_\mu}}{\Delta_\mu}\right)^2$, where 1_μ is a unit vector along the μ^{th} direction. A functional derivative with respect to $\phi_{[j_x,j_y,j_z]}$ yields,

$$\sum_{\mu=x,y,z} -C_\nu \frac{\phi_{[j_x,j_y,j_z]+1_\mu} + \phi_{[j_x,j_y,j_z]-1_\mu} - 2\phi_{[j_x,j_y,j_z]}}{\Delta^2_\mu} + a\phi_{[j_x,j_y,j_z]} = 0, \tag{A.11}$$

which yields second derivatives along each direction, as expected.

For points lying on the boundaries, some neighbors are missing. For instance, for points lying on the $x = L_x$, equivalently $j_x = N_x$, we have,

$$\begin{aligned} S_j = &\Delta_x\Delta_y\Delta_z\Bigg[\frac{1}{2}C_x\left(\frac{\phi_{[N_x,j_y,j_z]} - \phi_{[N_x-1,j_y,j_z]}}{\Delta_x}\right)^2 \\ &+ \sum_{\substack{\mu=y,z \\ \sigma=\pm1}} \frac{1}{2}C_\mu\left(\frac{\phi_{[N_x,j_y,j_z]} - \phi_{[N_x,j_y,j_z]-\sigma 1_\mu}}{\Delta_\mu}\right)^2\Bigg] + \Delta_y\Delta_z\left[\frac{1}{2}a^{s,x}\phi^2_{[N_x,j_y,j_z]}\right], \end{aligned} \tag{A.12}$$

$$\begin{aligned} \frac{\partial S}{\partial \eta_{[N_x,j_y,j_z]}} = &\Delta_x\Delta_y\Delta_z\left[\frac{C_x}{\Delta_x}\frac{\phi_{[N_x,j_y,j_z]} - \phi_{[N_x-1,j_y,j_z]}}{\Delta_x} + \sum_{\substack{\mu=y,z \\ \sigma=\pm1}} \frac{C_\mu}{\Delta_\mu}\frac{\phi_{[N_x,j_y,j_z]} - \phi_{[j_x,j_y,j_z]-\sigma 1_\mu}}{\Delta_\mu}\right] \\ &+ \Delta_y\Delta_z\left[a^{s,x}\phi_{[N_x,j_y,j_z]}\right] = 0 \\ \phi_{[N_x,j_y,j_z]} = &\frac{\left(\frac{C_x}{\Delta^2_x}\right)\phi_{[j_x-1,j_y,j_z]} + \sum_{\mu=y,z}\left(\frac{C_\mu}{\Delta^2_\mu}\right)\left(\phi_{[j_x,j_y,j_z]-1_\mu} + \phi_{[j_x,j_y,j_z]+1_\mu}\right) - \frac{a^{s,x}}{\Delta_x}}{\left(\frac{C_x}{\Delta^2_x}\right) + 2\left(\frac{C_\mu}{\Delta^2_\mu}\right)} \end{aligned} \tag{A.13}$$

where $j_\nu = m$ denotes the sites for which the discrete index of the ν^{th} coordinate equals m. The first term in the square brackets is $\sim \partial_x \phi/\Delta$, while the second one is $\sim \partial_\mu^2 \phi$. Consequently, in the continuum limit where $\Delta_\mu \to 0$, only the first term survives. The equations for the edges and the vertices may be obtained similarly.

Appendix B

Elasticity theory

An excellent reference to the theory of elasticity is found in Ref. [91], parts of which we describe here according to their relevance in this work.

B.1 Strain tensor

Beginning with two generic points $\boldsymbol{r}_{1,2}$ inside a solid with separation $d\boldsymbol{r}$, a deformation field $\boldsymbol{u}(\boldsymbol{r})$ is imposed. As a result, the separation between the points $\boldsymbol{r}_1$ and $\boldsymbol{r}_2$ is now given by,

$$dl^2 = \left(d\boldsymbol{r} + \boldsymbol{u}\left(\boldsymbol{r}_1\right) - \boldsymbol{u}\left(\boldsymbol{r}_2\right)\right)^2 \approx d\boldsymbol{r}^2 + \left(\frac{\partial u_i}{\partial x_j} + \frac{\partial u_j}{\partial x_i} + \frac{1}{2}\frac{\partial u_k}{\partial x_i}\frac{\partial u_k}{\partial x_j}\right) dx_i dx_j. \tag{B.1}$$

This motivates the definition of the strain tensor,

$$\varepsilon_{ij} = \frac{1}{2}\left(\frac{\partial u_i}{\partial x_j} + \frac{\partial u_j}{\partial x_i}\right), \tag{B.2}$$

where terms quadratic in the deformations are neglected, thereby forming the basis of linear elasticity. Note that the strain is symmetric $\varepsilon_{ij} = \varepsilon_{ji}$ and hence, it has six components in three dimensions.

B.2 Stress tensor

The forces acting on any plane and along any direction are described by the *symmetric* stress-tensor[1] $\sigma_{ij}(r)$. Specifically, the Cartesian components of the force acting on a plane perpendicular to the unit vector $\boldsymbol{n}$ is obtained from,

$$F_j = \sigma_{ij} n_i = \sigma_{ij} n_j. \tag{B.3}$$

Like the strain tensor, the stress tensor is also symmetric $\sigma_{ij} = \sigma_{ji}$. The diagonal elements of the stress tensor σ_{ij} determine the pressure along the axes, while the off-diagonal parts determine the shear components of the stress.

B.3 Hooke's Law

While we have introduced stress and strain independently, in reality, a strain field leads to a corresponding stress. The actual description of this relation hinges upon the microscopic properties of the solid. However, phenomenologically, the relation may be described using the Hooke's Law,

$$\sigma_{ij} = C_{ijkl} \varepsilon_{kl}, \tag{B.4}$$

which relates the stress σ_{ij} and strain ε_{kl} components linearly, via an elastic stiffness tensor C_{ijkl},

$$C_{ijkl} = \begin{bmatrix} C_{1111} & C_{1122} & C_{1133} & C_{1123} & C_{1113} & C_{1112} \\ C_{2211} & C_{2222} & C_{2233} & C_{2223} & C_{2213} & C_{2212} \\ C_{3311} & C_{3322} & C_{3333} & C_{3323} & C_{3313} & C_{3312} \\ C_{2311} & C_{2322} & C_{2333} & C_{2323} & C_{2313} & C_{2312} \\ C_{1311} & C_{1322} & C_{1333} & C_{1323} & C_{1313} & C_{1312} \\ C_{1211} & C_{1222} & C_{1233} & C_{1223} & C_{1213} & C_{1212} \end{bmatrix} \tag{B.5}$$

which is a 4^{th} rank tensor. From the symmetry of the strain and stress tensors, it follows that, $C_{ijkl} = C_{jikl} = C_{ijlk} = C_{klij}$. These symmetries constrain the elastic

[1] Latin indices denote 3-vectors.

modulus tensor to possess only twenty-one components. Depending on the physical symmetries of the solid, the number of independent components of the stiffness tensor is further reduced.

Before proceeding, we introduce the Voigt notation in which, employing the symmetries $C_{ijkl} = C_{klij}$, $\varepsilon_{ij} = \varepsilon_{ji}$, and $\sigma_{ij} = \sigma_{ji}$, the stress and strain are expressed as 6×1 vectors and the elasticity tensor is written as a symmetric 6×6 matrix,

$$\begin{bmatrix} \sigma_{11} \\ \sigma_{22} \\ \sigma_{33} \\ \sigma_{23} \\ \sigma_{31} \\ \sigma_{12} \end{bmatrix} = \begin{bmatrix} C_{11} & C_{12} & C_{13} & C_{14} & C_{15} & C_{16} \\ C_{12} & C_{22} & C_{23} & C_{24} & C_{25} & C_{26} \\ C_{13} & C_{23} & C_{33} & C_{34} & C_{35} & C_{36} \\ C_{14} & C_{24} & C_{34} & C_{44} & C_{45} & C_{46} \\ C_{15} & C_{25} & C_{35} & C_{45} & C_{55} & C_{56} \\ C_{16} & C_{26} & C_{36} & C_{46} & C_{56} & C_{66} \end{bmatrix} \begin{bmatrix} \varepsilon_{11} \\ \varepsilon_{22} \\ \varepsilon_{33} \\ 2\varepsilon_{23} \\ 2\varepsilon_{31} \\ 2\varepsilon_{12} \end{bmatrix}, \tag{B.6}$$

where, $\varepsilon_{11} = \varepsilon_{xx}$, $\varepsilon_{22} = \varepsilon_{yy}$, $\varepsilon_{33} = \varepsilon_{zz}$, $\varepsilon_{23} = \varepsilon_{yz}$, $\varepsilon_{31} = \varepsilon_{zx}$, and $\varepsilon_{12} = \varepsilon_{xy}$. These are often further shortened to $\varepsilon_1 = \varepsilon_{11}$, $\varepsilon_2 = \varepsilon_{22}$, $\varepsilon_3 = \varepsilon_{33}$, $\varepsilon_4 = 2\varepsilon_{23}$, $\varepsilon_5 = 2\varepsilon_{13}$, and $\varepsilon_6 = 2\varepsilon_{12}$.

In particular, for an isotropic solid, elastic stiffness tensor is specified by only two Lamé parameters λ, μ,

$$C_{\text{isotropic}} = \begin{bmatrix} \lambda + 2\mu & \lambda & \lambda & 0 & 0 & 0 \\ \lambda & \lambda + 2\mu & \lambda & 0 & 0 & 0 \\ \lambda & \lambda & \lambda + 2\mu & 0 & 0 & 0 \\ 0 & 0 & 0 & \mu & 0 & 0 \\ 0 & 0 & 0 & 0 & \mu & 0 \\ 0 & 0 & 0 & 0 & 0 & \mu \end{bmatrix}. \tag{B.7}$$

Alternatively, one may employ the Young′s modulus E and the Poisson′s ratio ν. For

an isotropic material, the elastic constants are related to these parameters by,

$$C_{11} = C_{22} = C_{33} = \lambda + 2\nu = \frac{E(1-\nu)}{(1+\nu)(1-2\nu)}, \tag{B.8a}$$

$$C_{12} = C_{13} = \lambda = \frac{E(\nu)}{(1+\nu)(1-2\nu)}, \tag{B.8b}$$

$$C_{44} = C_{55} = C_{66} = \frac{C_{11} - C_{12}}{2} = \mu = \frac{E}{2(1+\nu)} \tag{B.8c}$$

For a tetragonal crystal, after considering the invariance of the crystal structure under reflections about $[100], [010]$, and $[001]$ planes, and 90 degree rotations along the $c-$axis, one requires just five parameters. Specifically, using the Voigt notation, they are given by,

$$C_{\text{tetragonal}} = \begin{bmatrix} C_{11} & C_{12} & C_{13} & 0 & 0 & 0 \\ C_{12} & C_{11} & C_{13} & 0 & 0 & 0 \\ C_{13} & C_{13} & C_{33} & 0 & 0 & 0 \\ 0 & 0 & 0 & C_{44} & 0 & 0 \\ 0 & 0 & 0 & 0 & C_{44} & 0 \\ 0 & 0 & 0 & 0 & 0 & C_{66} \end{bmatrix}. \tag{B.9}$$

B.4 Elastic equation of motion

Defining $\boldsymbol{u}$ as the deformation at time t and spatial location $\boldsymbol{r}$, the Newton's second law for a body with mass density $\rho(\boldsymbol{r})$, is written as,

$$\int_\Omega d^3r \rho \partial_t^2 \boldsymbol{u}_i = \int_{\partial\Omega} dS \sigma_{ij} n_j = \int_\Omega d^3r \frac{\partial \sigma_{ij}}{\partial r_j}, \tag{B.10}$$

$$\therefore \int_\Omega d^3r \left(\rho \partial_t^2 \boldsymbol{u}_i - \frac{\partial \sigma_{ij}}{\partial r_j} \right) = 0 \implies \rho \partial_t^2 \boldsymbol{u}_i - \frac{\partial \sigma_{ij}}{\partial r_j} = \rho \partial_t^2 \boldsymbol{u}_i - C_{ijkl} \frac{\partial \varepsilon_{kl}}{\partial r_j} = 0, \tag{B.11}$$

where, the last line yields the equation of motion. Naturally, this leads to the identification of $\frac{\partial \sigma_{ij}}{\partial r_j}$ as the force density.

B.5 Elastic energy

The elastic potential energy is obtained by considering the work done by the internal forces acting on the net surface of the body,

$$\delta W = \int_\Omega d^3r \frac{\partial \sigma_{ij}}{\partial r_j}\delta u_i = \int_{\partial\Omega} dS\sigma_{ij}\underbrace{\delta u_i}_{=0} - \int_\Omega d^3r\sigma_{ij}\delta\varepsilon_{ij} = -\int_\Omega d^3r\frac{1}{2}C_{ijkl}\varepsilon_{ij}\varepsilon_{kl} \quad \text{(B.12)}$$

$$E = \int TdS - \int dW = \Delta Q + \frac{1}{2}C_{ijkl}\varepsilon_{ij}\varepsilon_{kl} + \sigma_{ij}\varepsilon_{ij}, \quad \text{(B.13)}$$

where, the last term is the contribution from the external stress which cannot be connected to the strains via the stiffness tensor. The second last line may be obtained by parametrizing the total deformation $u_i = su_i$ with $s \in [0,1]$, $du_i = u_i ds$, and then integrating over s. For crystals, the elastic stiffness tensor is directly related to the deformation potential $u_{a,i}\big(\frac{\partial^2 V_{a,b}}{\partial u_{a,i}\partial u_{b,j}}\big)u_{b,j} = -\varepsilon_{a,ik}\big(\frac{1}{2}r_k\frac{\partial^2 V_{a,b}}{\partial u_{a,i}\partial u_{b,j}}r_l\big)\varepsilon_{b,jl}$, where $\nabla = \boldsymbol{r}_a - \boldsymbol{r}_b$, corresponding to the deformations at sites a, b along directions i, j.

B.6 Structural transition

Here, we describe phase transitions in crystal lattices, characterized by the spontaneous deformation of the unit cell of the lattice in a certain direction. The elastic energy $\frac{1}{2}C_{ij}\varepsilon_i\varepsilon_j$, with the stiffness tensor C_{ij} being a symmetric tensor, can be diagonalised with an orthogonal matrix to yield, $F = \frac{1}{2}C_{ij}\varepsilon_i\varepsilon_i = \frac{1}{2}C_\alpha\varepsilon_\alpha^2$. For a crystal lattice to be stable, the elastic energy and thus, the eigenvalues of the elastic stiffness tensor, must be positive definite. This is embodied in the Born stability criterion. However, with the elastic constants being (indirectly) dependent on external control parameters, such as temperature, some eigenvalues for some specific momenta may decrease and vanish. This leads to unconstrained deformations with soft phonons corresponding to the modes with vanishing eigenvalues. Consequently, these soft modes lead to a structural instability associated with the symmetry of the soft mode [92, 93]. In particular, for the tetragonal to orthorhombic transition, with the high temperature tetragonal phase characterized

by the elastic stiffness tensor given by Eq.(B.9), the eigenvectors are [93],

$$
\begin{aligned}
e_1 &= \frac{1}{\sqrt{2}}(1,-1,0,0,0,0)^T, \\
e_2 &= \sqrt{\frac{4C_{13}}{(C_+ + C_-)^2 + 4}}\left(\frac{C_+ + C_-}{2C_{13}}, \frac{C_+ + C_-}{2C_{13}}, 1, 0, 0, 0\right)^T \\
e_3 &= \sqrt{\frac{4C_{13}}{(C_+ + C_-)^2 + 4}}\left(\frac{C_+ - C_-}{2C_{13}}, \frac{C_+ - C_-}{2C_{13}}, 1, 0, 0, 0\right)^T \\
e_4 &= (0,0,0,1,0,0)^T, \\
e_5 &= (0,0,0,0,1,0)^T, \\
e_6 &= (0,0,0,0,0,1)^T,
\end{aligned}
\tag{B.14}
$$

where,

$$
\begin{aligned}
&C_+ = C_{11} + C_{12} - C_{33}, \quad C_- = \sqrt{8C_{13}^2 + (C_{11} + C_{12} - C_{33})^2}, \\
&C_1 = C_{11} - C_{12}, \quad C_2 = \tfrac{C_+ - C_- + 2C_{33}}{2}, \quad C_3 = \tfrac{C_+ + C_- + 2C_{33}}{2}, \\
&C_4 = C_{44}, \quad C_5 = C_{44}, \quad C_6 = C_{66}.
\end{aligned}
\tag{B.15}
$$

For the tetragonal to orthorhombic structural transition, characterized by a B_{1g} deformation with inequivalent $x-$ and $y-$direction, the eigenvalue corresponding to the first eigenvector mentioned above, $C_{11} - C_{12}$, must vanish. In general, based on the symmetries of the disordered phase, a Ginzburg-Landau free energy may be formulated in terms of the strain fields, which allows for the general classification of the possible structural phase transitions [92, 93].

B.7 Plate theory: Approximate strain profile of a sample glued to a substrate

Here, we discuss the expected strain profile and provide an analytical approximation, which is used to provide the initial guess for the self-consistent finite-element-method based solution. Typically samples are glued to a substrate or attached to a piezo-electric layer. Since the sample and the substrate have different elastic constants, any strain must be accompanied by a proportionate bending to ensure interface continuity. Hence,

an accurate analysis of the elastic deformation would require the consideration of the varying strain profile along the thickness (transverse direction, across the layers) of the structure. For this purpose, we resort to analytical plate theory [94, 95] in which, as the material strains and bends, the cross-sectional areas remain flat and normal to the longitudinal axes of the plate, as shown in Fig. B.1. Additionally, line elements oriented perpendicular to the mid-plane do not deform, i.e., $\varepsilon_{zz} \to 0$. As a result, the strain is found to be linearly varying with depth ($z-$distance),

$$\varepsilon_{xx} = \bar{u}_{x,x} - \big(L - z\big)\bar{u}_{z,xx} = \frac{1}{\sqrt{2}}\big(\varepsilon_{A_{1g}} + \varepsilon_{B_{1g}}\big), \tag{B.16a}$$

$$\varepsilon_{yy} = \bar{u}_{y,y} - \big(L - z\big)\bar{u}_{z,yy} = \frac{1}{\sqrt{2}}\big(\varepsilon_{A_{1g}} - \varepsilon_{B_{1g}}\big) \tag{B.16b}$$

$$\varepsilon_{A_{1g}} = \frac{1}{\sqrt{2}}\big(\varepsilon_{xx} + \varepsilon_{yy}\big), \quad \varepsilon_{B_{1g}} = \frac{1}{\sqrt{2}}\big(\varepsilon_{xx} - \varepsilon_{yy}\big). \tag{B.16c}$$

Using the Dirichlet boundary condition at the sample-substrate interface $\varepsilon_{xx,z=L} =$

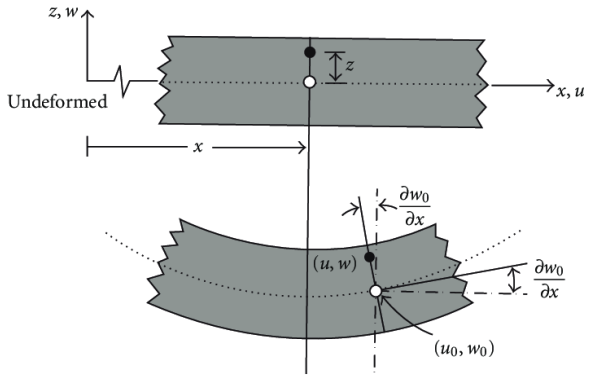

Figure B.1: Adapted from Ref. [3]: Schematic describing the extension and the consequent bending (exaggerated) of a composite structure. The strain varies linearly across the thickness and vanishes at the neutral plane, denoted by the subscript 0. Here $u_0 = \bar{u}_x$ and $w_0 = \bar{u}_z$ as in Eq. (B.16). At leading (linear) order in $\partial w_0/\partial_x$, the final position of the point (u_0, w_0) is $(u_0 - z\partial w_0/\partial_x, w_0)$.

$\varepsilon_{yy,z=L} = 0$, which is valid when the substrate is much larger and/or stiffer than the sample, we obtain $\bar{u}_{x,x} = \bar{u}_{y,y} = 0$. Consequently, $\varepsilon_{B_{1g},z} = \big(L - z\big)\big(\bar{u}_{z,xx} - \bar{u}_{z,yy}\big) =$

$\big(L-z\big)\varepsilon_{B_{1g},0}$. Hence, in plate theory, the action is given by,

$$S=\int_0^L dz\bigg[\frac{1}{2}C\varepsilon_{B_{1g},0}^2\big(L-z\big)^2+\frac{1}{2}a\eta^2-g_{\text{el-nem}}\eta\varepsilon_{B_{1g},0}\big(L-z\big)\bigg], \tag{B.17}$$

and the corresponding saddle-point equation is,

$$\frac{\partial S_\varepsilon}{\partial\varepsilon_{B_{1g},0}}=C\varepsilon_{B_{1g},0}\frac{L^3}{3}-g_{\text{el-nem}}\int_0^L dz\eta\big(L-z\big)=0, \tag{B.18}$$

where $\varepsilon_{B_{1g}}=\varepsilon_{B_{1g},0}\big(L-z\big)$ with the glued sample-substrate interface located at $z=L$. Under the plate-theoretic assumption, which is valid when the sample is thin (plate-like, but not film/membrane-like), the transverse strains with $z-$derivatives are neglected. A self-consistent solution of Eq.(B.18) is used as the seed for the self-consistent finite element method solution in the main text.

Appendix C

FEM critical temperature

Here, we present the convergence of the numerically found critical temperature, with varying number of lattice discretisation points $N = N_x = N_y$. To ensure equal discretisation along all the axes, we have chosen $N_z = \text{round}(NL/L_\parallel)$.

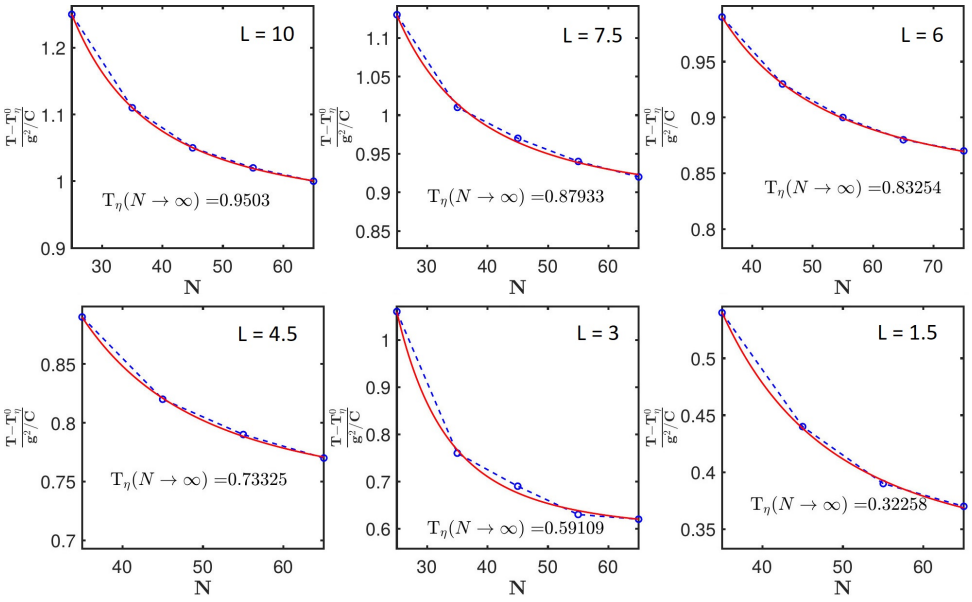

Figure C.1: The convergence of the critical temperatures with $N = N_x = N_y$, and $N_z = \text{round}(NL/L_\parallel)$, with $u_\eta = 0.1$, $b = 0.5 = 2b_x = 2b_y$, and $C = 0.5$. To extrapolate to the continuum regime, with $N \to \infty$, we have fit the numerically obtained data with the ansatz $T_\eta(N) = a + b(N^{-c})$ with $c \approx 1.9$, shown by the red lines. The actual critical temperature, given by the $N \to \infty$ limits of each fit, is specified in the panels.